IEEE Open Journal of the Communications Society

Received XX Month, XXXX; revised XX Month, XXXX; accepted XX Month, XXXX; Date of publication XX Month, XXXX; date of current version 12 August, 2025.

Digital Object Identifier 10.1109/OJCOMS.2024.011100

From Sub-6 GHz to Millimeter-Wave: Dynamic Indoor Measurements, Channel Characteristics and Performance Evaluation

FARUK PASIC[1] *(Graduate Student Member, IEEE)*, MARIAM MUSSBAH[1,2], MARKUS HOFER[3] *(Member, IEEE)*, SEBASTIAN CABAN[1], STEFAN SCHWARZ[1] *(Senior Member, IEEE)*, THOMAS ZEMEN[3] *(Senior Member, IEEE)*, MARKUS RUPP[1] *(Fellow, IEEE)* AND CHRISTOPH F. MECKLENBRÄUKER[1] *(Senior Member, IEEE)*

[1]Institute of Telecommunications, TU Wien, Vienna, Austria
[2]Christian Doppler Laboratory for Digital Twin assisted AI for sustainable Radio Access Networks
[3]AIT Austrian Institute of Technology, Vienna, Austria

CORRESPONDING AUTHOR: Faruk Pasic (e-mail: faruk.pasic@tuwien.ac.at).

The work of M. Mussbah has been funded by the Christian Doppler Laboratory for Digital Twin assisted AI for sustainable Radio Access Networks, Institute of Telecommunications, TU Wien. The work of M. Hofer and T. Zemen was funded within the Principal Scientist grant Dependable Wireless 6G Communication Systems (DEDICATE 6G). Part of this work has been presented at IEEE 97th Vehicular Technology Conference (VTC2023-Spring) [1].

ABSTRACT Future wireless communication systems will extend the employed frequency bands from sub-6 GHz to millimeter wave (mmWave) bands to achieve higher data rates. To investigate different propagation characteristics between sub-6 GHz and mmWave bands in indoor environments, it is essential to conduct multi-band channel measurements. In this work, we perform dynamic channel measurements using a measurement setup that enables comparing sub-6 GHz and mmWave bands in a fair manner. Measurements are conducted in an indoor environment at center frequencies of 2.55 GHz and 25.5 GHz at transmitter velocities of 50 km/h and 100 km/h. Based on the acquired measurement data, we conduct a comparative analysis of the multi-band propagation characteristics. Specifically, we compare the channels in terms of root-mean-square (RMS) delay spread, Rician K-factor, RMS Doppler spread and RMS angular spread. Additionally, we evaluate the system performance at both frequency bands in terms of achievable spectral efficiency derived from the measured channels. Our results show that differences in delay-domain parameters (RMS delay spread and Rician K-factor) and angular-domain (RMS angular spread) are relatively minor and are unlikely to significantly impact system design. However, the RMS Doppler spread increases proportionally with carrier frequency and transmitter velocity, causing channel state information (CSI) at mmWave frequencies to become outdated much more rapidly. This imposes a substantial performance limitation for mmWave systems in dynamic scenarios.

INDEX TERMS millimeter-wave, sub-6 GHz, radio propagation, channel measurement, indoor scenario, performance evaluation.

I. INTRODUCTION

THE amount of global mobile data traffic is growing rapidly and is expected to reach around 450 exabytes per month by 2030 [2]. A significant portion of this growth is driven by emerging indoor wireless applications, such as ultra-high-definition video streaming, high-resolution virtual/augmented reality (VR/AR) and environmental monitoring [3]. These applications require extremely high data rates, which are difficult to support with conventional systems operating in the sub-6 GHz frequency bands due to spectrum limitations. A promising solution to meet this growing demand for high transmission rates is the utilization

of mmWave frequency bands (24 GHz – 300 GHz) [4], which offer significantly larger bandwidths compared to sub-6 GHz systems [5], [6]. Thus, the development of mmWave communication systems is attracting increasingly more attention [7].

While mmWave systems offer significant benefits in terms of available bandwidth and achievable data rates, these advantages come with notable challenges. In contrast to sub-6 GHz frequencies, the propagation characteristics of mmWave signals differ substantially due to their much shorter wavelengths. For instance, a mmWave signal at 25 GHz experiences an isotropic path loss approximately 20 dB higher than a signal at 2.5 GHz, as described by the Friis free-space equation [8]. Additionally, mmWave signals are more sensitive to dynamic blockage from obstacles such as the human body, further limiting their reliability and coverage [9].

Therefore, mmWave systems are increasingly being integrated with sub-6 GHz systems, which benefit from more favorable propagation conditions and therefore offer more reliable coverage. Leveraging both frequency bands in a cooperative multi-band communication system allows for increased overall capacity while maintaining robust coverage and reliability [10]. Furthermore, reliable out-of-band information from the sub-6 GHz band can be exploited to aid link establishment and beam alignment in the mmWave band [11]–[15]. Since the channel characteristics fundamentally determine the performance limits of a communication system, it is essential to understand how these characteristics evolve across frequency bands - from sub-6 GHz to mmWave. Achieving this requires carefully designed channel measurements across sub-6 GHz and mmWave bands to ensure fair and consistent comparisons. The insights derived from such multi-band studies are crucial for developing accurate multi-band channel models and guiding the design and deployment of future multi-band communication systems.

A. State-of-the-Art

Numerous comparative multi-band studies based on channel measurements in various environments have already been presented in the literature. For instance, the work in [16] investigates multi-band channel characteristics at 4 and 61 GHz in outdoor line-of-sight (LOS) and non-line-of-sight (NLOS) conditions. In [17], the authors analyze channel characteristics across 3.3, 6.5, 15 and 28 GHz using measurements from outdoor urban micro and outdoor-to-indoor scenarios. Several studies also examine sub-6 GHz and mmWave channels in vehicular scenarios. Specifically, [18]–[21] focus on vehicle-to-vehicle (V2V) scenarios, while [22]–[25] investigate vehicle-to-infrastructure (V2I) scenarios. Additionally, multi-band propagation characteristics in industrial environments are analyzed in [26], [27].

In indoor environments, sub-6 GHz and mmWave channels have largely been characterized through separate measurement campaigns, which limits the direct comparability between the two frequency bands. Numerous studies have focused on sub-6 GHz indoor channel measurements [28]–[40], while the majority of mmWave indoor measurement and modeling efforts have been conducted at 60 GHz [41]–[47] and 25-28 GHz bands [48]–[56].

In addition to these separate investigations, several multi-band indoor measurement studies have emerged [57]–[63]. For example, Anderson *et al.* [57] analyze path loss and multipath delay spread at 2.5 and 60 GHz based on measured data. Koymen *et al.* [58] present results from indoor measurements conducted at 2.9 and 29 GHz, including analysis of path loss, excess delay and root-mean-square (RMS) delay spread. Furthermore, Virk *et al.* [59] compare power angular spectra at 2, 15, 28 and 60 GHz. The authors in [60] study the frequency dependency of the RMS delay spread using multi-frequency measurements ranging from 2 to 86 GHz in indoor, outdoor and outdoor-to-indoor scenarios. De Jong *et al.* [61] report on double-directional indoor measurements conducted at seven frequency bands between 2.4 and 61 GHz, analyzing path loss, shadow fading, RMS delay spread and angular spreads. Jiang *et al.* [62] present indoor and outdoor measurements at 3.5 GHz and 28 GHz, focusing on the number of clusters, inter-cluster intervals and intra-cluster RMS delay spread. Moreover, Zhang *et al.* [63] investigate the composite and cluster-level channel characteristics based on measurements obtained in a classroom and a hall indoor scenarios at 2-4 GHz, 9-11 GHz and 27-29 GHz.

The indoor measurements discussed above primarily focus on a single analysis domain - either the delay domain or the angular domain - with only [58], [61], [63] addressing both. Additionally, most of these studies are conducted in static indoor scenarios, without accounting for movement of the transmitter, receiver, or scattering objects. Another often overlooked aspect is the relative positioning of antennas across different frequency bands. A physical separation of just a few centimeters can correspond to multiple wavelengths at mmWave frequencies, introducing spatial offsets that may affect small-scale fading and significantly distort the resulting channel statistics.

B. Contributions

This paper makes the following key contributions:

- We conduct multi-band channel measurements with a moving transmit antenna using the measurement setup proposed in [64]. Our measurement setup enables dynamic channel measurements at different frequency bands while maintaining identical transmit and receive antenna positions as well as the same transmit antenna velocity. This ensures repeatability and allows for a fair comparison of time-varying channel characteristics across different frequency bands. The measurements have been conducted at the center frequency of 2.55 GHz and 25.5 GHz and transmitter velocity of 50 km/h and 100 km/h at 126 different spatial positions in an indoor environment. This scenario reflects private industrial networks operating indoors at both sub-

6 GHz and mmWave frequencies. In this context, high mobility refers to fast-moving and rotating mechanical components of industrial machines that are intended to communicate with static control systems.

- We perform a comparative statistical evaluation between sub-6 GHz and mmWave frequency bands based on a set of collected measurements, extending our previous work from [1]. Our evaluation considers three domains of analysis: delay, Doppler and angular. Specifically, we compare different frequency bands in terms of RMS delay spread, RMS Doppler spread and Rician K-factor. Furthermore, we exploit time snapshots as elements of a virtual antenna array (VAA), enabling a comparative analysis of RMS angular spreads between sub-6 GHz and mmWave channels. Moreover, we provide a comprehensive comparison of estimated channel parameters - specifically RMS delay spread and RMS angular spread - based on existing indoor measurement studies, alongside our own measurement results.
- Using measured channel data, we evaluate the system performance in terms of achievable spectral efficiency (SE) at both, sub-6 GHz and mmWave bands. Utilizing the VAA, we analyze the impact of the number of antennas and the use of precoding on performance in time-varying channels.

C. Organization

The remainder of the paper is structured as follows. Section II describes the measurement setup and outlines the procedure used to conduct comparable multi-band channel measurements in an indoor environment. Section III details the statistical evaluation of the channel parameters and presents the results in terms of RMS delay spread, Rician K-factor, RMS Doppler spread and RMS angular spread. Section IV evaluates the system performance based on the measurement data, focusing on the achievable SE. Finally, Section V concludes the paper.

D. Notation

The superscript $(\cdot)^{(\mathrm{b})}$ represents frequency-band dependent values, where $\mathrm{b} \in \{\mathrm{s}, \mathrm{m}\}$, with s referring to the sub-6 GHz and m to the mmWave band. Scalars are denoted by x, vectors by bold lowercase letters $\mathbf{x}$ and matrices by bold uppercase letters $\mathbf{X}$. The superscripts $(\cdot)^{\mathrm{T}}$ and $(\cdot)^{\mathrm{H}}$ represent transpose and Hermitian transpose, respectively. The Euclidean norm is represented by $\|\cdot\|$.

II. Multi-band Channel Measurements

In this section, we present our multi-band indoor channel measurements. We begin by describing the measurement setup in Section II-A. Subsequently, in Section II-B, we outline the measurement campaign and the procedure used to ensure comparable multi-band channel measurements in an indoor environment.

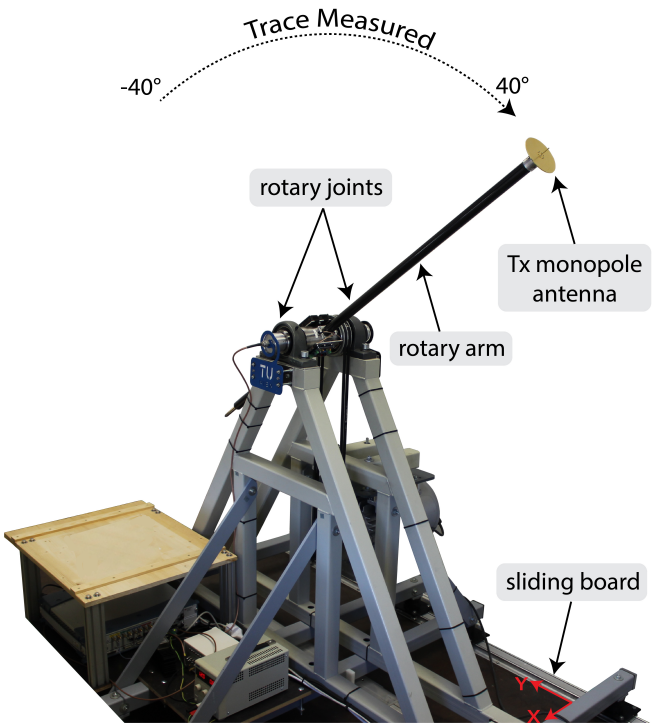

FIGURE 1. The measurement setup is designed to compare sub-6 GHz and mmWave channels in a controlled dynamic environment [64]. At the end of the rotating arm, either a sub-6 GHz antenna or a mmWave transmitter with an integrated antenna is mounted.

A. Measurement Setup

Our measurement setup, as detailed in [64], employs a moving transmitter and a static receiver, enabling repeatable sub-6 GHz and mmWave channel measurements at high velocities of up to 400 km/h. The moving transmitter is mounted on a rotary unit [65]–[67] that spins a 1 m long arm around a central axis at a constant speed, with an antenna attached to the arm's end (see Fig. 1). The rotary unit incorporates a trigger mechanism which initiates a measurement once per revolution by generating a pulse at a configurable angle of the arm. Two rotary joints deliver signals from a fixed source to the rotating transmit antenna. The entire rotary unit is mounted on a sliding platform, allowing lateral movement of 33 cm along the x-axis and 81 cm along the y-axis. This lateral mobility of the rotary unit enables measurements at different transmitter positions within the plane. The accuracy and repeatability of the proposed setup have been quantified in [68], demonstrating its capability to repeat experiments with negligible uncertainty.

Sub-6 GHz: The transmit signal is generated directly at a center frequency of $f_{\mathrm{c}}^{(\mathrm{s})} = 2.55\,\mathrm{GHz}$ using the arbitrary waveform generator (AWG) (Keysight M8195A), as illustrated in Fig. 2a. The signal is then passed via the rotary joint to the omnidirectional monopole antenna that is fixed at the end of the rotating arm (see Fig. 3a). At the receiver, a horn antenna with half-power beamwidth (HPBW) of 30° is used. The received signal is first amplified by a low

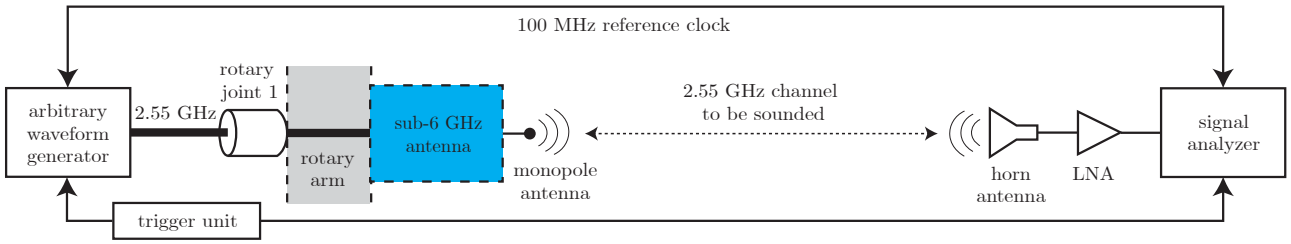

(a) Sub-6 GHz: The transmit signal is generated at a center frequency of $f_{\mathrm{c}}^{(\mathrm{s})} = 2.55\,\mathrm{GHz}$ and passed via a rotary joint to a monopole antenna.

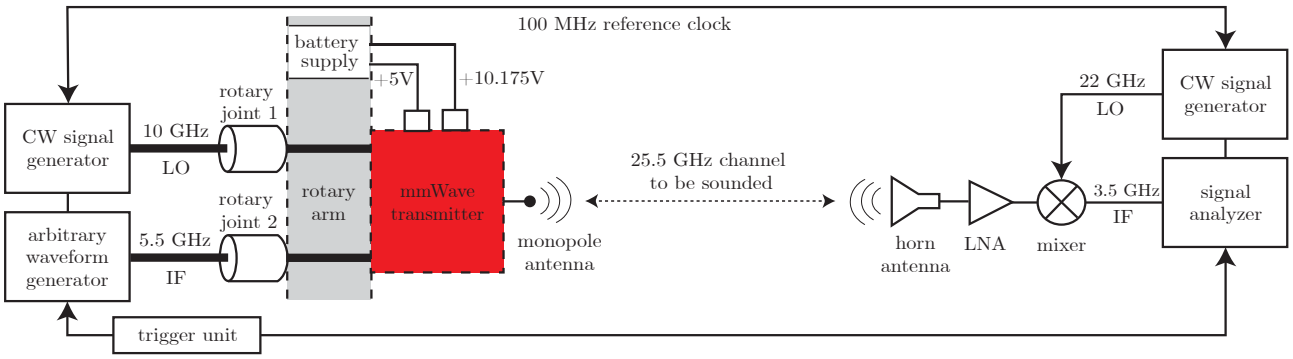

(b) Millimeter-wave: The transmit signal is generated at an intermediate frequency (IF) of $f_{\mathrm{IF}}^{(\mathrm{m})} = 5.5\,\mathrm{GHz}$, passed via a rotary joint to a mmWave transmitter, where it is up-converted to a center frequency of $f_{\mathrm{c}}^{(\mathrm{m})} = 25.5\,\mathrm{GHz}$ and then passed to a monopole antenna.

FIGURE 2. The sub-6 GHz and mmWave measurement setups utilize a moving transmitter and a static receiver.

noise amplifier (LNA) (Mini-Circuits ZX60-P105LN+) and subsequently captured by a signal analyzer (Guzik Digitizer ADP7104), which serves as the receiver. The captured signal, in the form of I/Q samples, is subsequently transferred from the signal analyzer to a hard disk for storage.

Millimeter Wave: Direct signal transmission to the rotating transmit antenna is not feasible due to the frequency limitations of the rotary joints used (Sage Labs 344F), which support signal frequencies only up to 12.4 GHz. To enable mmWave signal transmission, a custom-build mmWave transmitter with an integrated omnidirectional monopole antenna is employed and mounted at the end of the rotating arm, as detailed in [64], [69] and illustrated in Fig. 3b.

The mmWave transmitter performs frequency up-conversion based on intermediate frequency (IF) and local oscillator (LO) inputs. The IF signal is generated by the AWG, while the LO is provided by a continuous wave (CW) signal generator (R&S SMA100B). Both signals are delivered to the mmWave transmitter via two rotary joints, as shown in Fig. 2b. An internal frequency doubler within the mmWave transmitter doubles the LO frequency before mixing it with the IF signal, resulting in a radio frequency (RF) output defined as

$$f_{\mathrm{c}}^{(\mathrm{m})} = 2f_{\mathrm{LO}}^{(\mathrm{m})} + f_{\mathrm{IF}}^{(\mathrm{m})}. \tag{1}$$

Specifically, with an IF of $f_{\mathrm{IF}}^{(\mathrm{m})} = 5.5\,\mathrm{GHz}$ and a LO frequency of $f_{\mathrm{LO}}^{(\mathrm{m})} = 10\,\mathrm{GHz}$, the resulting RF center frequency is $f_{\mathrm{c}}^{(\mathrm{m})} = 25.5\,\mathrm{GHz}$.

As in the sub-6 GHz setup, the mmWave receiver employs a horn antenna with HPBW of 30°. To ensure a fair comparison between the sub-6 GHz and mmWave measurements, antennas with comparable radiation patterns are employed, i.e., monopole antennas at the transmitter and horn antennas at the receiver. The received signal is first amplified by an LNA (RF-Lambda R24G40GSB), then down-converted using a mixer (Mini-Circuits ZMDB-44H-K+), with the LO signal provided by a CW signal generator (R&S SMF100A). The resulting IF signal is subsequently fed to the signal analyzer.

Synchronization: Precise frequency synchronization is achieved by interconnecting the AWG (transmitter) and the signal analyzer (receiver) with a 100 MHz reference. Similarly, precise time synchronization is ensured by distributing the trigger pulse from the trigger unit to both the AWG and the signal analyzer via coaxial cables.

B. Measurement Campaign

Using the measurement setup from Section II-A, we conduct wireless channel measurements in an indoor environment (see Fig. 4). The transmit antenna is placed in a smaller room and is moving with a constant velocity at the rotary unit (see Fig. 1). The receive antenna is positioned in a larger room approximately 7.5 m away from the transmit antenna and remains static on a laboratory table. We conduct measurements at center frequencies of 2.55 GHz and 25.5 GHz, velocities of 50 km/h and 100 km/h, and different positions

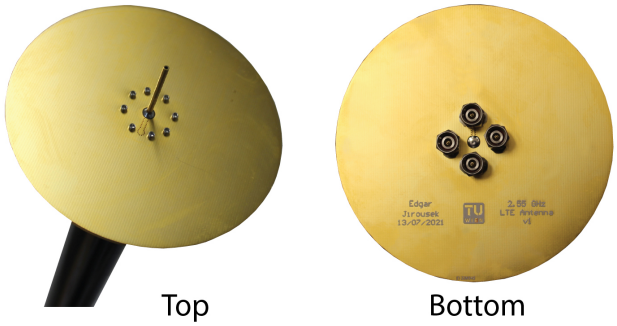

(a) Sub-6 GHz: monopole antenna (left) and connectors (right) with one connector for transmit signal and three connectors for mechanical stability.

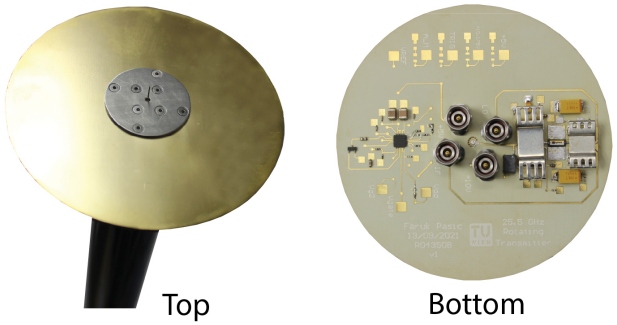

(b) Millimeter-wave: monopole antenna (left) and transmitter (right) with connectors for IF and LO signals, along with two additional connectors for power supply.

FIGURE 3. The sub-6 GHz and mmWave setups employ a monopole transmit antenna.

TABLE 1. Channel Sounding Parameters

Parameter	Value			
Bandwidth B [MHz]	100			
Delay Resolution $\Delta\tau$ [ns]	10			
Number of Symbols K	50 000			
Number of Snapshots K_{snap}	500			
Number of x-axis Positions N_{x}	7			
Number of y-axis Positions N_{y}	18			
Transmit Power P_{T} [dBm]	10			
Measured Arc Segment $\Delta\zeta$ [°]	80			
Rotation Radius r_{arm} [m]	1			
Snapshots per Stat. Region L_{snap}	250			
Scenario-specific Parameter	**A**	**B**	**C**	**D**
Carrier Frequency f_{c} [GHz]	2.55	2.55	25.5	25.5
Wavelength λ [cm]	11.7	11.7	1.17	1.17
Tx Velocity v_{Tx} [km/h]	50	100	50	100
Number of Subcarriers N	200	100	200	100
Subcarrier Spacing $\triangle f$ [kHz]	500	1000	500	1000
Symbol Duration t_{s} [µs]	2	1	2	1
Snapshot Duration t_{snap} [µs]	200	100	200	100
Measurement Duration t_{m} [ms]	100	50	100	50
Max. Doppler Shift $\nu_{\max}$ [Hz]	118.1	236.2	1181	2362

according to the rectangular grid shown in Fig. 4. Measurement scenarios and corresponding parameters are provided in Tab. 1. Specifically, scenarios A-D combine two carrier frequencies with two velocities: scenario A - 2.55 GHz, 50 km/h; scenario B - 2.55 GHz, 100 km/h; scenario C - 25.5 GHz, 50 km/h; scenario D - 25.5 GHz, 100 km/h.

To compare measurements at different velocities and different frequency bands in a fair manner, we satisfy two criteria:

- Firstly, we need to ensure a static fading environment. To achieve this, we carry out the entire measurement campaign within a 2-hour time window, during which there is no human presence or movement in the room.
- Secondly, we need to ensure that the channel measurements in all scenarios are conducted along the identical transmit antenna trace and at the identical receive antenna position. To achieve this, the rotating transmit antenna moves along the same trace (from $-40°$ to $40°$), transmitting an equal number of symbols for all scenarios. Specifically, a short symbol duration of 1 µs is used for high-velocity measurements, while a long symbol duration of 2 µs is selected for low-velocity measurements (see Tab. 1).

Note that the angular position of $0°$ corresponds to the direction normal to the floor. Given the measured arc segment of $\Delta\zeta = 80°$ and a rotation radius of $r_{\text{arm}} = 1\,\text{m}$, the corresponding arc length is given by

$$l_{\text{m}} = r_{\text{arm}}\,\Delta\zeta\,\frac{\pi}{180} \approx 1.4\,\text{m}. \tag{2}$$

Measurement Procedure: We transmit a sequence of $K = 50\,000$ identical orthogonal frequency-division multiplexing (OFDM) transmit symbols as channel-sounding signal while the transmit antenna moves from $-40°$ to $40°$ at the rotary unit. The transmit symbols are designed using a Zadoff-Chu sequence to keep the peak-to-average power ratio (PAPR) low [70]. A frequency-domain transmit symbol is given by

$$\mathrm{x}^{(\mathrm{b})}[n] = e^{-\mathrm{j}\pi\frac{n^2}{N^{(\mathrm{b})}}}, \tag{3}$$

where $n \in \{-N^{(\mathrm{b})}/2, \ldots, N^{(\mathrm{b})}/2 - 1\}$ denotes the subcarrier index. At the receiver, the measurement sequence is grouped into $K_{\text{snap}} = 500$ snapshots, each consisting of 100 OFDM symbols. This grouping is made under the assumption that the wireless channel between the moving transmit antenna and the static receive antenna remains time-invariant over the duration of a single snapshot. Further, the first OFDM symbol of each snapshot is discarded, as it serves as a cyclic prefix. To enhance the signal-to-noise ratio (SNR), the remaining 99 symbols are averaged, resulting in an SNR improvement of approximately 20 dB. Following OFDM processing, the wireless channel is estimated across all subcarriers using least-squares (LS) estimation as follows:

$$\widetilde{\mathrm{H}}_{w}^{(\mathrm{b})}[n,k] = \frac{\mathrm{y}^{(\mathrm{b})}[n,k]}{\mathrm{x}^{(\mathrm{b})}[n]\,\widetilde{\mathrm{H}}_{\text{cal}}^{(\mathrm{b})}[n]} \tag{4}$$

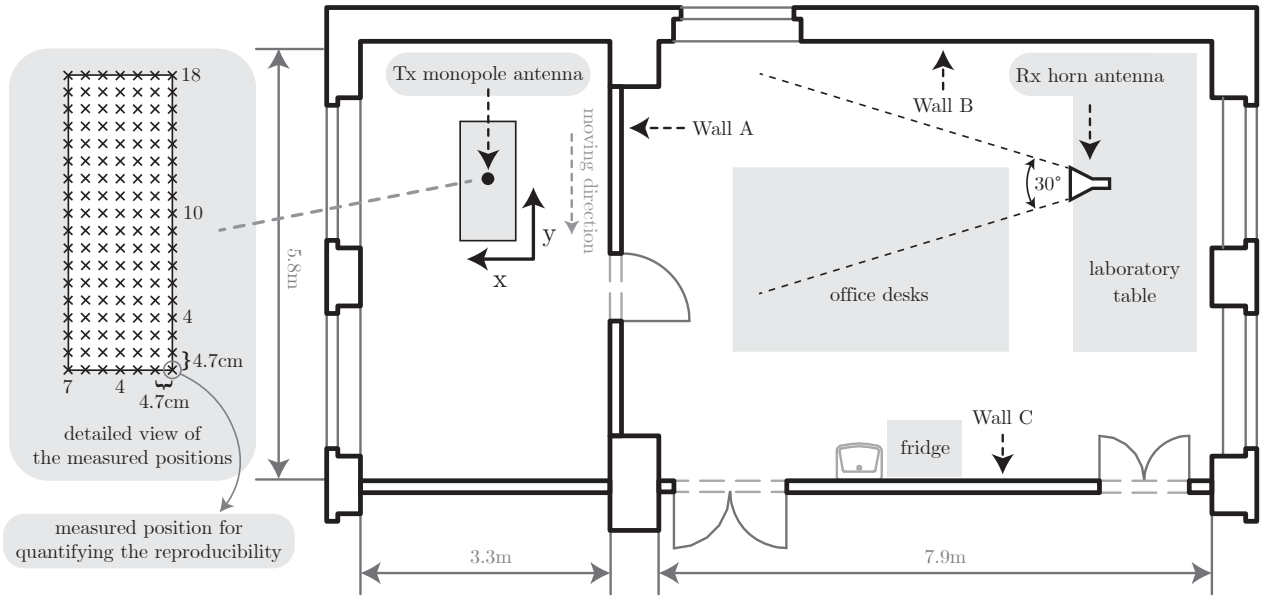

FIGURE 4. **Measured indoor environment [1]. The moving transmit antenna and the statical receive antenna are located in neighboring rooms. The detailed view of the measured positions shows the transmit antenna position when passing 0° of the measured arc segment.**

where $\mathrm{x}^{(\mathrm{b})}[n]$ is the known Zadoff-Chu OFDM transmit symbol, $\mathrm{y}^{(\mathrm{b})}[n,k]$ is the received OFDM symbol after averaging and $\widetilde{\mathrm{H}}_{\mathrm{cal}}^{(\mathrm{b})}[n]$ represents the calibration transfer function of the RF chains for each subcarrier. The calibration function is obtained by directly connecting the transmitter and receiver using attenuators and measuring the channel transfer function (CTF). This procedure yields the time-variant CTF $\widetilde{\mathrm{H}}_{w}^{(\mathrm{b})}[n,k]$ for frequency (subcarriers) $n \in \{-N^{(\mathrm{b})}/2,\ldots,N^{(\mathrm{b})}/2-1\}$ and snapshots $k \in \{-K_{\mathrm{snap}}/2,\ldots,K_{\mathrm{snap}}/2-1\}$. Note that the obtained time-variant CTF $\widetilde{\mathrm{H}}_{w}^{(\mathrm{b})}[n,k]$ corresponds to a single transmitter position in space (see Fig. 4). Measurements are conducted at N_{x} positions along the x-axis and N_{y} positions along the y-axis, according to the rectangular grid from Fig. 4, where $\mathrm{x} \in \{1,\ldots,N_{\mathrm{x}}\}$ and $\mathrm{y} \in \{1,\ldots,N_{\mathrm{y}}\}$. For readability, the spatial position indices x and y are omitted and will be explicitly introduced when necessary.

SINR Estimation: In addition to the comparative analysis of the channel characteristics in Section III, we also assess the system performance in terms of SE in Section IV. Since SE fundamentally depends on the signal-to-interference-and-noise ratio (SINR), we require a reliable estimation of the SINR. This allows us to quantify the impact of interference and noise on achievable data rates.

Our measurement setup operates at center frequencies of 2.55 GHz and 25.5 GHz, corresponding to the fifth generation (5G) new radio (NR) frequency bands n7 and n258, respectively [71]. Operating within these standardized bands exposes the system to potential interference from external transmitters, as the setup is not deployed in an anechoic environment with RF isolation. To enable SINR estimation, we set the central subcarrier of the transmit symbol $\mathrm{x}^{(\mathrm{b})}[n]$ to zero, i.e., $\mathrm{x}^{(\mathrm{b})}[0]=0$. At the receiver, the SINR is then estimated from the received symbols for each spatial position by

$$\widetilde{\gamma}_{wI}^{(\mathrm{b})}[k] = \frac{\underbrace{\frac{1}{N^{(\mathrm{b})}-1}\sum_{\substack{\forall n \\ n\neq 0}}\left|\mathrm{y}^{(\mathrm{b})}[n,k]\right|^2}_{\text{signal + interference + noise}} - \underbrace{\widetilde{\sigma}^2_{wI^{(\mathrm{b})}}[k]}_{\text{interference + noise}}}{\underbrace{\widetilde{\sigma}^2_{wI^{(\mathrm{b})}}[k]}_{\text{interference + noise}}}, \tag{5}$$

where $\widetilde{\sigma}^2_{wI^{(\mathrm{b})}}[k] = \left|\mathrm{y}^{(\mathrm{b})}[0,k]\right|^2$ denotes the estimated power of the noise-plus-interference. After estimating the SINR, the received symbol at the central subcarrier is approximated using nearest-neighbor interpolation, i.e., $\mathrm{y}^{(\mathrm{b})}[0,k] = \mathrm{y}^{(\mathrm{b})}[1,k]$. The estimated SINR for the sub-6 GHz band is $\widetilde{\gamma}_{wI}^{(\mathrm{s})}[k] \approx 22\,\mathrm{dB}$, while for the mmWave band it is $\widetilde{\gamma}_{wI}^{(\mathrm{m})}[k] \approx 11\,\mathrm{dB}$.

III. Comparative Channel Analysis

In this section, we perform a comparative analysis of channel parameters between the sub-6 GHz and mmWave bands. We begin by post-processing the measurement data in Section III-A to obtain the time-variant local scattering function (LSF), power delay profile (PDP) and Doppler power spectral density (DSD). This is followed by delay-domain analysis in Section III-B, Doppler-domain analysis in Section III-C and angular-domain analysis in Section III-D, each accompanied by the corresponding results. Finally, Section III-E compares our results with those reported in the existing literature.

A. Measurement Data Post-Processing

Every measured time-variant CTF is contaminated by additive noise, which can bias the estimation of channel parameters. To mitigate this, we employ the following approach to remove the only-noise samples from the measured CTFs. We first convert the time-variant CTF $\widetilde{\mathrm{H}}_w^{(\mathrm{b})}[n,k]$ to the delay domain $\widetilde{\mathrm{H}}_w^{(\mathrm{b})}[\tau,k]$, using the inverse discrete Fourier transform (IDFT). For each snapshot, the noise floor $\mathcal{N}_{\mathrm{dB}}^{(\mathrm{b})}[\tau]$ is estimated independently by the median, following the procedure described in [72]. A threshold $\Delta\mathcal{N}_{\mathrm{dB}}^{(\mathrm{b})}$ is then applied and all the values below $\overline{\mathcal{N}}_{\mathrm{dB}}^{(\mathrm{b})}[\tau]=\mathcal{N}_{\mathrm{dB}}^{(\mathrm{b})}[\tau]+\Delta\mathcal{N}_{\mathrm{dB}}^{(\mathrm{b})}$ are set to zero, as follows:

$$\widetilde{\mathrm{H}}^{(\mathrm{b})}[\tau,k]=\begin{cases}\widetilde{\mathrm{H}}_w^{(\mathrm{b})}[\tau,k], & \text{if } \left|\widetilde{\mathrm{H}}_w^{(\mathrm{b})}[\tau,k]\right|^2_{\mathrm{dB}}\geq\overline{\mathcal{N}}_{\mathrm{dB}}^{(\mathrm{b})}[\tau]\\ 0, & \text{else}\end{cases} \tag{6}$$

As detailed in [73], setting a threshold reduces the probability of interpreting noise samples as valid signal components. In our analysis, we use a fixed threshold of $\Delta\mathcal{N}_{\mathrm{dB}}^{(\mathrm{b})}=6\,\mathrm{dB}$ for all scenarios, following one of the evaluated options presented in [73]. Finally, we transform the time-variant channel impulse response (CIR) $\widetilde{\mathrm{H}}^{(\mathrm{b})}[\tau,k]$ back to the frequency domain $\widetilde{\mathrm{H}}^{(\mathrm{b})}[n,k]$, using the discrete Fourier transform (DFT).

To analyze the time-frequency dispersion, we characterize the channel by the LSF using the concept from [74], [75]. For each measured scenario, we assume that the channel is locally stationary across the entire frequency range and over a window of $L_{\mathrm{snap}}=250$ snapshots. Given the measured arc length of $l_{\mathrm{m}}\approx 1.4\,\mathrm{m}$ and a total number of snapshots of $K_{\mathrm{snap}}=500$, the window of L_{snap} snapshots correspond to a spatial segment of

$$l_{\mathrm{snap}}=\frac{l_{\mathrm{m}}}{K_{\mathrm{snap}}}L_{\mathrm{snap}}=70\,\mathrm{cm}. \tag{7}$$

This assumption is supported by a stationarity analysis of similar data collected in the same measurement environment presented in [76], which identified a spatial region of 70 cm with collinearity values above 0.8 for both sub-6 GHz and mmWave frequency bands. Note that the collinearity metric is bounded between 0 and 1, where a value of 1 corresponds to a stationary channel. The time index of each stationarity region is $l\in\{1,\ldots,K_{\mathrm{snap}}/L_{\mathrm{snap}}\}$ and corresponds to the center of the stationarity region. To obtain multiple independent spectral estimates from CTFs, we use the following multitaper based estimator

$$\widetilde{\mathcal{H}}_{(\mathrm{G}_w)}^{(\mathrm{b})}[l;\tau,\nu]=\sum_{n=-\frac{N^{(\mathrm{b})}}{2}}^{\frac{N^{(\mathrm{b})}}{2}-1}\sum_{k=-\frac{K_{\mathrm{snap}}}{2}}^{\frac{K_{\mathrm{snap}}}{2}-1}\widetilde{\mathrm{H}}^{(\mathrm{b})}[n,k+l\,L_{\mathrm{snap}}]\cdot\mathrm{G}_w^{(\mathrm{b})}[n,k]\,e^{\mathrm{j}2\pi(\nu k-\tau n)} \tag{8}$$

where $\nu\in\{-L_{\mathrm{snap}}/2,\ldots,L_{\mathrm{snap}}/2-1\}$ denotes the Doppler index and $\tau\in\{0,\ldots,N^{(\mathrm{b})}-1\}$ represents the delay index. The delay and Doppler shift resolutions are given by $\Delta\tau=1/B$ and $\Delta\nu^{(\mathrm{b})}=1/\left(L_{\mathrm{snap}}t_{\mathrm{snap}}^{(\mathrm{b})}\right)$. By applying the window function $\mathrm{G}_w^{(\mathrm{b})}[n,k]$, the considered CTF is confined to the single stationarity region l, thereby minimizing the influence of other stationarity regions [75]. Without the window, contributions from neighboring stationarity regions could leak into the stationarity region of interest l, potentially corrupting the estimate. Therefore, the window functions $\mathrm{G}_w^{(\mathrm{b})}[n,k]$ should be well localized within the designated support region $\left[-N^{(\mathrm{b})}/2,N^{(\mathrm{b})}/2-1\right]\times[-K_{\mathrm{snap}}/2,K_{\mathrm{snap}}/2-1]$. To ensure this, we apply the discrete-time equivalent of the separable window function used in [75], i.e.,

$$\mathrm{G}_w^{(\mathrm{b})}[n,k]=u_i\left[n+N^{(\mathrm{b})}/2\right]\hat{u}_j\left[k+K_{\mathrm{snap}}/2\right], \tag{9}$$

where $w=iJ+j$, $i\in\{0,\ldots,I-1\}$ and $j\in\{0,\ldots,J-1\}$. The sequences $u_i[n]$ and $\hat{u}_j[k]$ are selected as the discrete prolate spheroidal sequences (DPSS) [77]. The number of tapers in the frequency and time domains is set to $I=3$ and $J=3$, respectively [78]. The LSFs of each window are then averaged to produce $\widetilde{\mathrm{S}}^{(\mathrm{b})}[l;\tau,\nu]$, as given by

$$\widetilde{\mathrm{S}}^{(\mathrm{b})}[l;\tau,\nu]=\frac{1}{IJ}\sum_{w=0}^{IJ-1}\left|\widetilde{\mathcal{H}}_{(\mathrm{G}_w)}^{(\mathrm{b})}[l;\tau,\nu]\right|^2. \tag{10}$$

To allow for better comparability between different frequency bands and different velocities, we introduce the normalized Doppler shift ν_{N} as

$$\nu_{\mathrm{N}}=\frac{\nu}{f_{\mathrm{c}}^{(\mathrm{b})}v_{\mathrm{Tx}}^{(\mathrm{b})}}\left[\frac{\mathrm{Hz}}{\mathrm{Hz}\frac{\mathrm{m}}{\mathrm{s}}}=\frac{\mathrm{s}}{\mathrm{m}}\right], \tag{11}$$

where ν denotes the Doppler shift, $f_{\mathrm{c}}^{(\mathrm{b})}$ represents the carrier frequency and $v_{\mathrm{Tx}}^{(\mathrm{b})}$ is the transmit antenna velocity. This way, the LSF $\widetilde{\mathrm{S}}^{(\mathrm{b})}[l;\tau,\nu_{\mathrm{N}}]$ is confined to same interval of ν_{N} for all measured scenarios. As the LSF from (10) corresponds to a single spatial transmitter position, we introduce here the spatial indices x and y. The LSF of each stationarity region l and each spatial position x and y are then averaged to produce the average LSF $\widetilde{\mathrm{S}}_{\mathrm{avg}}^{(\mathrm{b})}[\tau,\nu_{\mathrm{N}}]$, given by

$$\widetilde{\mathrm{S}}_{\mathrm{avg}}^{(\mathrm{b})}[\tau,\nu_{\mathrm{N}}]=\frac{1}{\frac{K_{\mathrm{snap}}}{L_{\mathrm{snap}}}N_{\mathrm{x}}N_{\mathrm{y}}}\sum_{l=1}^{\frac{K_{\mathrm{snap}}}{L_{\mathrm{snap}}}}\sum_{\mathrm{x}=1}^{N_{\mathrm{x}}}\sum_{\mathrm{y}=1}^{N_{\mathrm{y}}}\widetilde{\mathrm{S}}^{(\mathrm{b})}[l,\mathrm{x},\mathrm{y};\tau,\nu_{\mathrm{N}}]. \tag{12}$$

The averaged LSF $\widetilde{\mathrm{S}}_{\mathrm{avg}}^{(\mathrm{b})}[\tau,\nu_{\mathrm{N}}]$ is shown in Fig. 5. Note that the magnitude of $\widetilde{\mathrm{S}}_{\mathrm{avg}}^{(\mathrm{b})}[\tau,\nu_{\mathrm{N}}]$ is normalized such that its maximum value corresponds to 0 dB. We highlight the following observations. Firstly, the averaged LSF $\widetilde{\mathrm{S}}_{\mathrm{avg}}^{(\mathrm{b})}[\tau,\nu_{\mathrm{N}}]$ remains invariant with respect to the transmit antenna velocity. Therefore, scenarios A and B exhibit nearly identical behavior, as do scenarios C and D. Secondly, the averaged LSFs show comparable characteristics across the different frequency bands: the majority of the power is concentrated within the delay values between approximately 20 and 80 ns and normalized Doppler shifts ranging from -3 to

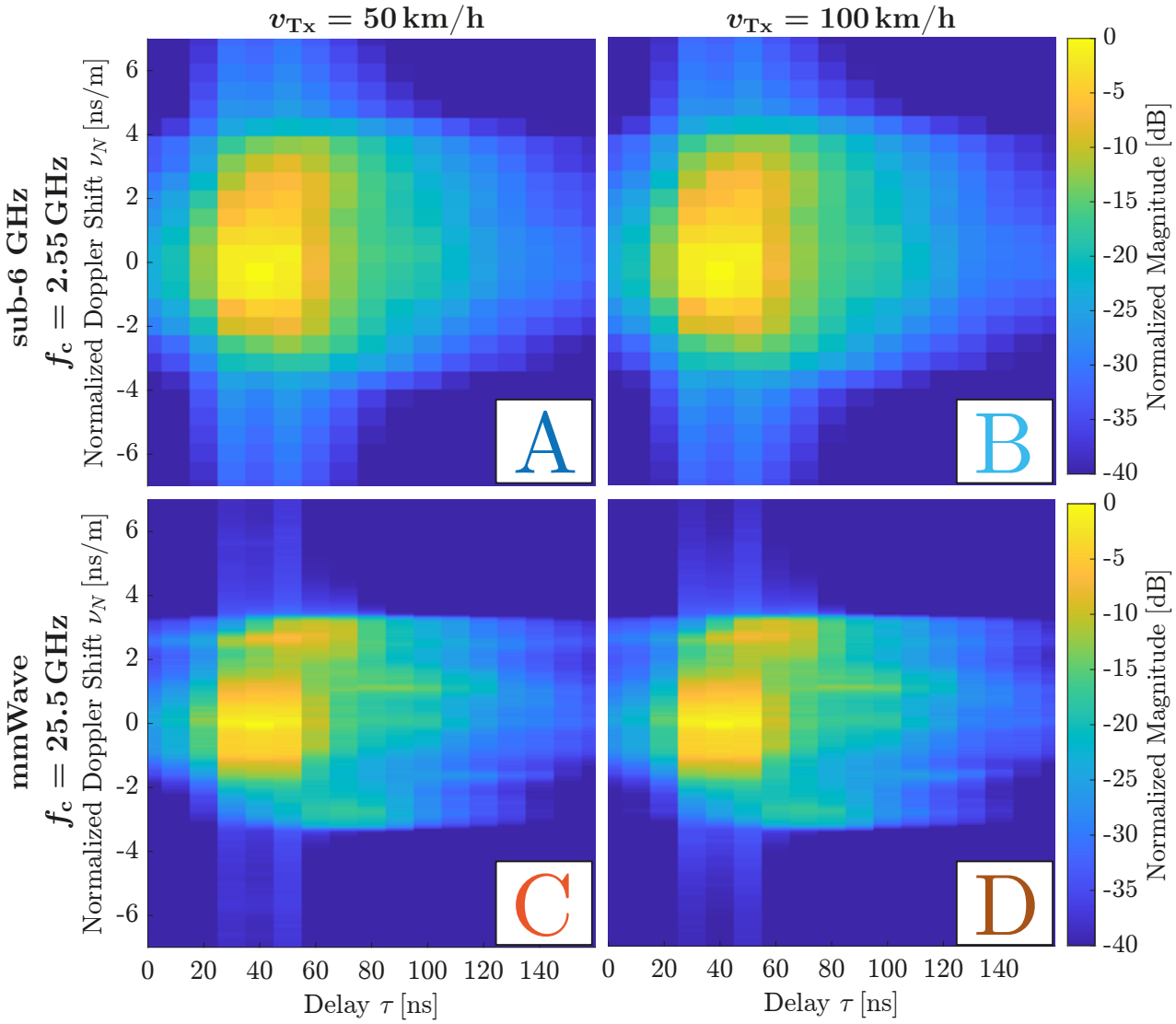

FIGURE 5. **The averaged LSF (parameterized by the normalized Doppler) remains effectively invariant with respect to the transmit antenna velocity: scenarios A and B exhibit nearly identical behavior, as do scenarios C and D. The averaged LSFs show comparable characteristics across the different frequency bands.**

4 ns/m. Nevertheless, subtle differences between the sub-6 GHz and mmWave bands can be observed. In addition to the strongest channel component around (40 ns, 0 ns/m), the mmWave scenarios (C and D) exhibit further distinct multi-path components located around (60 ns, 2.5 ns/m) and (80 ns, 1 ns/m). This phenomenon may be attributed to the fact that certain surfaces in the environment reflect mmWave signals more efficiently, producing detectable multipath components that are not present in the sub-6 GHz band. Moreover, the channel power at mmWave frequencies decays more rapidly with delay and Doppler shift compared to the sub-6 GHz scenarios.

After that, we calculate the PDP as an estimate of the expectation of the LSF over the Doppler domain, as follows:

$$\widetilde{\mathrm{P}}^{(\mathrm{b})}\left[l;\tau\right] = \frac{1}{L_{\mathrm{snap}}} \sum_{\forall \nu_{\mathrm{N}}} \widetilde{\mathrm{S}}^{(\mathrm{b})}\left[l;\tau,\nu_{\mathrm{N}}\right] \tag{13}$$

Furthermore, we calculate the DSD as an estimate of the expectation of the LSF over the delay domain, as follows:

$$\widetilde{\mathrm{D}}^{(\mathrm{b})}\left[l;\nu_{\mathrm{N}}\right] = \frac{1}{N^{(\mathrm{b})}} \sum_{\forall \tau} \widetilde{\mathrm{S}}^{(\mathrm{b})}\left[l;\tau,\nu_{\mathrm{N}}\right] \tag{14}$$

To allow for better comparability between different frequency bands, we normalize the power of $\widetilde{\mathrm{P}}^{(\mathrm{b})}\left[l;\tau\right]$ and $\widetilde{\mathrm{D}}^{(\mathrm{b})}\left[l;\nu_{\mathrm{N}}\right]$ so that their maximum values correspond to 0 dB. Furthermore, we define the dynamic range (DR) as the difference between the maximum power and the estimated noise floor, increased by the applied threshold. Since the DR varies across frequency bands due to differences in measurement equipment, we standardize it by selecting the smallest DR observed, ensuring a fair comparison across all scenarios. Specifically, we set the DR to 20 dB for all scenarios and set all values outside this range to zero.

B. Delay-Domain Analysis

We calculate the RMS delay spread $\sigma_\tau^{(\mathrm{b})}[l]$ as second-order moment of $\widetilde{\mathrm{P}}^{(\mathrm{b})}[l;\tau]$. The RMS delay is inversely related to the coherence bandwidth of the channel and it quantifies the extent of the delay dispersion of the multipath components arriving at the receiver [79]. The RMS delay spread is given by

$$\sigma_\tau^{(\mathrm{b})}[l] = \sqrt{\frac{\sum\limits_{\forall\tau}\tau^2\widetilde{\mathrm{P}}^{(\mathrm{b})}[l;\tau]}{\sum\limits_{\forall\tau}\widetilde{\mathrm{P}}^{(\mathrm{b})}[l;\tau]} - \left(\frac{\sum\limits_{\forall\tau}\tau\widetilde{\mathrm{P}}^{(\mathrm{b})}[l;\tau]}{\sum\limits_{\forall\tau}\widetilde{\mathrm{P}}^{(\mathrm{b})}[l;\tau]}\right)^2}. \quad (15)$$

Based on the estimated RMS delay spread, we derive the coherence bandwidth according to Fleury's uncertainty relationship [80]:

$$B_{\mathrm{coh}}^{(\mathrm{b})} \gtrsim \frac{1}{2\pi\sigma_\tau^{(\mathrm{b})}} \quad (16)$$

Furthermore, we estimate the Rician K-factor, which is another important parameter to characterize frequency-selectivity of the channel [79]. To estimate the K-factor, we use the technique introduced in [81], based on the method of moments (MoM) [82]. First, we calculate the power of the time-variant channel $\widetilde{\mathrm{H}}^{(\mathrm{b})}[l;n,k]$ for the stationarity region l as

$$\widetilde{P}_{\mathrm{H}}^{(\mathrm{b})}[l;n,k] = \left|\widetilde{\mathrm{H}}^{(\mathrm{b})}[l;n,k]\right|^2. \quad (17)$$

The first moment, or the average power of the time-variant channel, is given as

$$\overline{P}_{\mathrm{H}}^{(\mathrm{b})}[l] = \frac{1}{N^{(\mathrm{b})}L_{\mathrm{snap}}} \sum_{n=-\frac{N^{(\mathrm{b})}}{2}}^{\frac{N^{(\mathrm{b})}}{2}-1} \sum_{k=-\frac{L_{\mathrm{snap}}}{2}}^{\frac{L_{\mathrm{snap}}}{2}-1} \widetilde{P}_{\mathrm{H}}^{(\mathrm{b})}[l;n,k] \quad (18)$$

and the second moment of interest is the RMS fluctuation of $\widetilde{P}_{\mathrm{H}}^{(\mathrm{b})}[l;n,k]$ about $\overline{P}_{\mathrm{H}}^{(\mathrm{b})}[l]$ given by

$$v_{\mathrm{H}}^{(\mathrm{b})}[l] = \sqrt{\frac{1}{N^{(\mathrm{b})}L_{\mathrm{snap}}} \sum_{n=-\frac{N^{(\mathrm{b})}}{2}}^{\frac{N^{(\mathrm{b})}}{2}-1} \sum_{k=-\frac{L_{\mathrm{snap}}}{2}}^{\frac{L_{\mathrm{snap}}}{2}-1} \left(\dot{P}_{\mathrm{H}}^{(\mathrm{b})}[l;n,k]\right)^2}, \quad (19)$$

with

$$\dot{P}_{\mathrm{H}}^{(\mathrm{b})}[l;n,k] = \widetilde{P}_{\mathrm{H}}^{(\mathrm{b})}[l;n,k] - \overline{P}_{\mathrm{H}}^{(\mathrm{b})}[l]. \quad (20)$$

Next, the power of the constant channel term is computed as

$$\left|V_{\mathrm{H}}^{(\mathrm{b})}[l]\right|^2 = \sqrt{\left(\overline{P}_{\mathrm{H}}^{(\mathrm{b})}[l]\right)^2 - \left(v_{\mathrm{H}}^{(\mathrm{b})}[l]\right)^2} \quad (21)$$

and the power of the fluctuating channel term is given by

$$\left(\sigma_{\mathrm{H}}^{(\mathrm{b})}[l]\right)^2 = \overline{P}_{\mathrm{H}}^{(\mathrm{b})}[l] - \left|V_{\mathrm{H}}^{(\mathrm{b})}[l]\right|^2. \quad (22)$$

Finally, the estimated K-factor for the l-th stationarity region is given by the ratio of the constant to the fluctuating channel term, expressed as

$$\kappa^{(\mathrm{b})}[l] = \frac{\left|V_{\mathrm{H}}^{(\mathrm{b})}[l]\right|^2}{\left(\sigma_{\mathrm{H}}^{(\mathrm{b})}[l]\right)^2}. \quad (23)$$

We statistically evaluate the RMS delay spread and Rician K-factor across all stationarity regions and spatial positions. Specifically, we plot in Fig. 6 the empirical cumulative distribution function (CDF) of the RMS delay spread $\sigma_\tau^{(\mathrm{b})}[l,\mathrm{x},\mathrm{y}]$ (Fig. 6a) and the Rician K-factor $\kappa^{(\mathrm{b})}[l,\mathrm{x},\mathrm{y}]$ (Fig. 6b), considering all stationarity regions l and spatial positions x and y. The corresponding mean and standard deviation values for the different scenarios are summarized in Tab. 2.

We observe that sub-6 GHz and mmWave scenarios exhibit similar RMS delay spread values. Specifically, at mmWave frequencies, the mean RMS delay spread is approximately 1.48 ns (10%) larger compared to the sub-6 GHz band. This can be explained by Fig. 5, where the mmWave channel exhibits additional multipath components. Nevertheless, this difference in mean RMS delay spread is negligible at system level and is not expected to have a significant impact on system design considerations. Both frequency bands also show comparable standard deviation values, around 1 ns. Moreover, for the sub-6 GHz band, the coherence bandwidth is $B_{\mathrm{coh}}^{(\mathrm{s})} \gtrsim 14.69$ MHz at 50 km/h and $B_{\mathrm{coh}}^{(\mathrm{s})} \gtrsim 15.02$ MHz at 100 km/h. For the mmWave band, the coherence bandwidth is $B_{\mathrm{coh}}^{(\mathrm{m})} \gtrsim 12.59$ MHz at 50 km/h and $B_{\mathrm{coh}}^{(\mathrm{m})} \gtrsim 12.60$ MHz at 100 km/h. As expected, the coherence bandwidth is slightly larger for sub-6 GHz, since it is inversely proportional to the RMS delay spread.

Similarly, the mean K-factor values are comparable across the frequency bands, although the sub-6 GHz scenarios exhibit a slightly higher value - approximately 1.88 dB larger than the mmWave scenarios. This behavior is consistent with the RMS delay spread trends, as an increase in RMS delay spread typically corresponds to a decrease in the K-factor and vice versa. Again, this difference in mean K-factor is not critical for system design in the considered NLOS scenario. Furthermore, most estimated K-factor values lie below 0 dB, which is expected given the presence of wall A between transmitter and receiver. The standard deviation values for the K-factor are also similar, although the mmWave bands exhibit a slightly lower variability of approximately 2.6 dB.

C. Doppler-Domain Analysis

For the Doppler-domain analysis, we calculate the RMS Doppler spread $\sigma_\nu^{(\mathrm{b})}[l]$ and the normalized RMS Doppler spread $\sigma_{\nu_{\mathrm{N}}}^{(\mathrm{b})}[l]$ as the second-order moments of $\widetilde{\mathrm{D}}^{(\mathrm{b})}[l;\nu]$ and $\widetilde{\mathrm{D}}^{(\mathrm{b})}[l;\nu_{\mathrm{N}}]$, respectively. The RMS Doppler spread is inversely related to the coherence time of the channel, which indicates the rate of temporal variation [79]. The RMS Doppler spread is given by

$$\sigma_\nu^{(\mathrm{b})}[l] = \sqrt{\frac{\sum\limits_{\forall\nu}\nu^2\widetilde{\mathrm{D}}^{(\mathrm{b})}[l;\nu]}{\sum\limits_{\forall\nu}\widetilde{\mathrm{D}}^{(\mathrm{b})}[l;\nu]} - \left(\frac{\sum\limits_{\forall\nu}\nu\widetilde{\mathrm{D}}^{(\mathrm{b})}[l;\nu]}{\sum\limits_{\forall\nu}\widetilde{\mathrm{D}}^{(\mathrm{b})}[l;\nu]}\right)^2} \quad (24)$$

TABLE 2. Evaluated Channel Parameters

Frequency	Velocity (Scenario)	Parameter											
		σ_τ [ns]		κ [dB]		σ_ν [Hz]		σ_{ν_N} [ns/m]		ϑ [°]		σ_ϑ [°]	
		Mean	Std.	Mean	Std.	Mean	Std.	Mean	Std.	Mean	Std.	Mean	Std.
sub-6 GHz	50 km/h (A)	14.02	1.12	-1.95	3.46	48.02	6.08	1.35	0.17	-5.68	7.89	28.10	3.33
	100 km/h (B)	14.02	1.08	-1.96	3.29	96.03	12.10	1.35	0.17	-5.69	7.91	28.08	3.33
mmWave	50 km/h (C)	15.50	1.13	-3.83	2.49	394.66	60.56	1.11	0.17	1.38	10.46	27.79	4.32
	100 km/h (D)	15.55	1.14	-3.74	2.69	785.26	117.70	1.10	0.16	1.72	10.12	28.18	4.31

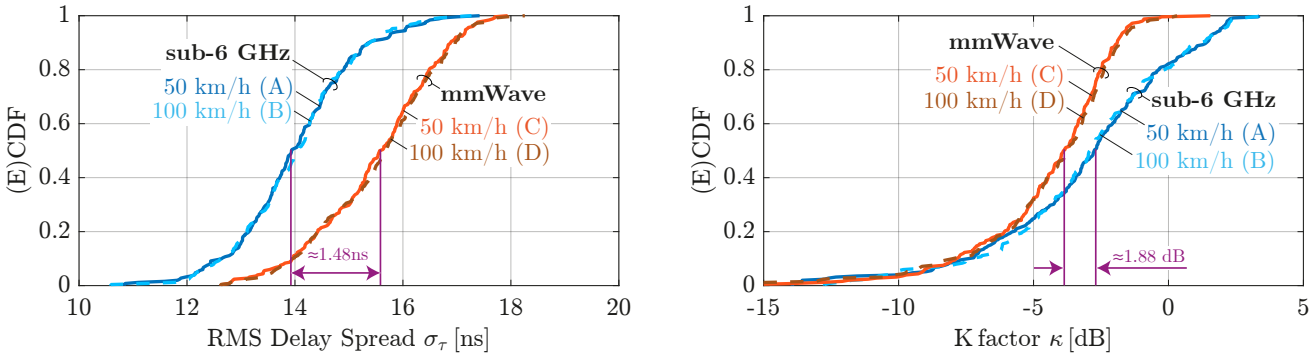

FIGURE 6. The RMS delay spread and K-factor values are similar for the sub-6 GHz and mmWave scenarios and remain almost invariant with regard to the transmitter velocity.

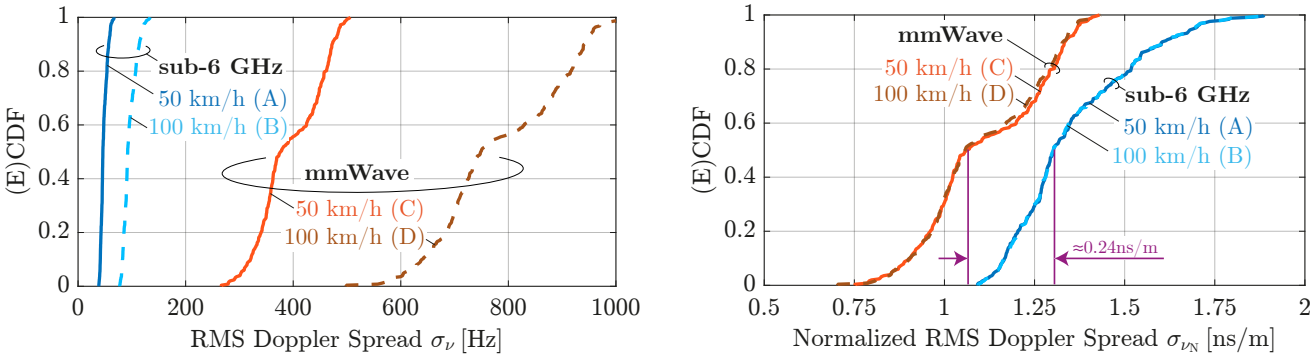

FIGURE 7. The RMS Doppler spread scales proportionally with the carrier frequency and the corresponding transmitter's velocity. The normalized RMS Doppler spreads are comparable across the frequency bands and are almost invariant with regard to the transmitter velocity.

and its normalized version is given by

$$\sigma^{(\mathrm{b})}_{\nu_\mathrm{N}}[l] = \sqrt{\frac{\sum\limits_{\forall \nu_\mathrm{N}} \nu_\mathrm{N}^2 \widetilde{\mathrm{D}}^{(\mathrm{b})}[l;\nu_\mathrm{N}]}{\sum\limits_{\forall \nu_\mathrm{N}} \widetilde{\mathrm{D}}^{(\mathrm{b})}[l;\nu_\mathrm{N}]} - \left(\frac{\sum\limits_{\forall \nu_\mathrm{N}} \nu_\mathrm{N} \widetilde{\mathrm{D}}^{(\mathrm{b})}[l;\nu_\mathrm{N}]}{\sum\limits_{\forall \nu_\mathrm{N}} \widetilde{\mathrm{D}}^{(\mathrm{b})}[l;\nu_\mathrm{N}]}\right)^2}. \tag{25}$$

Based on the estimated RMS Doppler spread, we quantify the coherence time according to Fleury's uncertainty relationship [80]:

$$t^{(\mathrm{b})}_{\mathrm{coh}} \gtrsim \frac{1}{2\pi\sigma^{(\mathrm{b})}_{\nu}} \tag{26}$$

We statistically evaluate the RMS Doppler spread across all stationarity regions and spatial positions. Specifically, Fig. 7 depicts the empirical CDF of the RMS Doppler spread $\sigma^{(\mathrm{b})}_{\nu}[l,\mathrm{x},\mathrm{y}]$ (Fig. 7a) and the normalized RMS Doppler spread $\sigma^{(\mathrm{b})}_{\nu_\mathrm{N}}[l,\mathrm{x},\mathrm{y}]$ (Fig. 7b), considering all stationarity regions l and spatial positions x and y. The corresponding mean and standard deviation values for the different scenarios are summarized in Tab. 2.

As expected, the RMS Doppler spread scales proportionally with the carrier frequency and the corresponding transmitter's velocity. Consequently, Scenario A exhibits

the smallest mean RMS Doppler spread, while Scenario D shows the largest mean values. This trend is similarly observed in the standard deviation values. Moreover, for the sub-6 GHz band, the coherence time is $t_{\text{coh}}^{(\text{s})} \gtrsim 4.11\,\text{ms}$ at 50 km/h and $t_{\text{coh}}^{(\text{s})} \gtrsim 2.05\,\text{ms}$ at 100 km/h. For the mmWave band, the coherence time is $t_{\text{coh}}^{(\text{m})} \gtrsim 0.59\,\text{ms}$ at 50 km/h and $t_{\text{coh}}^{(\text{m})} \gtrsim 0.31\,\text{ms}$ at 100 km/h. Consistent with its inverse relation to the RMS Doppler spread, the coherence time in the mmWave band is significantly shorter than in the sub-6 GHz band. Additionally, doubling the transmit antenna velocity roughly halves the coherence time in both bands.

However, consistent with the behavior of the frequency-selective parameters, the mean values of the normalized RMS Doppler spread are comparable across the frequency bands. Specifically, the sub-6 GHz scenarios show a slightly higher mean value - approximately 0.24 ns/m (21%) larger - compared to the mmWave scenarios. This observation aligns with Fig. 5, where both bands concentrate the strongest channel component around 0 ns/m, but the mmWave channels demonstrate a slightly faster decay in the Doppler domain. The faster power decay of the mmWave multipath components in the Doppler domain can be attributed to the predominance of specular rather than diffuse components in the mmWave band. In contrast, sub-6 GHz channels exhibit richer scattering with stronger diffuse contributions, resulting in a slower power decay in the Doppler domain.

In Fig. 7b, a noticeable curvature appears in the CDF of the normalized mmWave RMS Doppler spread in the 50%–60% range. This effect arises from the presence of two distinct clusters: one centered around 1 ns/m and another around 1.3 ns/m. The lower cluster corresponds to channel realizations where distinct multipath components at higher Doppler frequencies (around 3 ns/m) are absent, leading to a normalized RMS Doppler spread close to 1 ns/m. Conversely, when such higher-Doppler components are present, the normalized RMS Doppler spread shifts toward the higher cluster around 1.3 ns/m.

Due to the spatial filtering imposed by the highly directive receive horn antennas, the mean normalized RMS Doppler spread corresponds to approximately 40% and 33% of the maximum normalized RMS Doppler shift ($\nu_{\text{N,max}} = 3.33$ ns/m) for the sub-6 GHz and mmWave scenarios, respectively. The standard deviation values of the normalized RMS Doppler spread are also comparable, approximately 0.17 ns/m for both frequency bands.

Moreover, K-factor values as well as delay and Doppler spreads are almost invariant with regard to the transmitter's velocity, despite measurements being conducted at different times. Hence, there is a significant agreement between different scenarios within the same frequency band. This confirms the high accuracy and repeatability of the proposed measurement testbed.

D. Angular-Domain Analysis

We further perform a comparative analysis in the azimuth angular domain. Using the reciprocity principle, we model the moving omnidirectional transmit antenna as a VAA [79]. Specifically, we interpret time-domain snapshots as spatial samples, i.e., as virtual transmit antenna elements (see Fig. 8). Given the static fading environment (see Section II-B), we assume that the channel remains constant during the acquisition of the considered spatial samples. Given the arc length of $l_{\text{m}} \approx 1.4\,\text{m}$ and $K_{\text{snap}} = 500$ total measured snapshots, the spatial distance between two consecutive snapshots is given by

$$\Delta d_{\text{snap}} = l_{\text{m}} / K_{\text{snap}} \approx 2.8\,\text{mm}. \tag{27}$$

To achieve an effective antenna spacing close to $\Delta d^{(\text{b})} = 0.5\,\lambda^{(\text{b})}$, we select every $\Delta k_{\text{snap}}^{(\text{s})} = 20$ snapshot in the sub-6 GHz band and every $\Delta k_{\text{snap}}^{(\text{m})} = 2$ snapshot in the mmWave band. This ensures comparable normalized antenna spacing across the bands. Thus, we construct an approximately[1] uniform linear VAA in the azimuth plane, denoted by

$$\widetilde{\mathbf{h}}^{(\text{b})}[n] = \widetilde{\mathrm{H}}^{(\text{b})}\left[n, k_{\text{center}} + \Delta k_{\text{snap}}^{(\text{b})} \mathbf{d}^{(\text{b})}\right] \in \mathbb{C}^{1 \times M_{\text{Tx}}^{(\text{b})}}, \tag{28}$$

where the antenna element positions are given by the vector

$$\mathbf{d}^{(\text{b})} = \left\{0, 1, \ldots, M_{\text{Tx}}^{(\text{b})} - 1\right\} - M_{\text{Tx}}^{(\text{b})}/2 + 0.5. \tag{29}$$

Given that $k \in \{-K_{\text{snap}}/2, \ldots, K_{\text{snap}}/2 - 1\}$, the central snapshot index of the VAA is chosen as $k_{\text{center}} = 0$, corresponding to an angular position of approximately $0°$. In this analysis, we consider the VAA with $M_{\text{Tx}}^{(\text{b})} = 8$ virtual transmit antenna elements. To ensure consistent angular resolution and maintain a fair comparison across bands, we use the same number of elements for both frequency bands, i.e., $M_{\text{Tx}}^{(\text{s})} = M_{\text{Tx}}^{(\text{m})} = 8$. Note that only a single receive antenna is used in the measurement setup $\left(M_{\text{Rx}}^{(\text{b})} = 1\right)$. This modeling enables us to perform angular-domain processing and beamforming analysis using the time-domain measurements as spatially structured input.

We employ then the Bartlett beamformer [83] to perform beamforming analysis. For a uniform linear array (ULA) with $M_{\text{Tx}}^{(\text{b})} = 8$ elements, the HPBW of the Bartlett beamformer is approximately given by [83]

$$\text{HPBW} \approx 2 \arcsin\left(0.891 \frac{1}{M_{\text{Tx}}^{(\text{b})}}\right) = 12.78°. \tag{30}$$

In the considered indoor scenario, the RMS angular spread is expected to exceed this beamwidth due to rich multipath propagation caused by reflections from walls and other objects. As a result, the Bartlett beamformer provides sufficient angular resolution to capture the structure of the dominant angular components in the channel. We firstly stack the channel coefficients for all subcarriers and all transmit antennas

[1]Note that for $M_{\text{Tx}}^{(\text{b})} = 8$ antennas, the arc causes the VAA to exhibit up to approximately 10% non-uniformity in the azimuth plane.

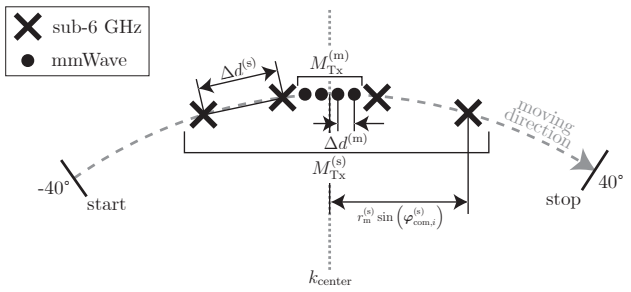

FIGURE 8. **Time-domain snapshots are interpreted as virtual transmit antenna elements, enabling us to perform angular-domain processing and beamforming analysis. The central snapshot index of the VAA is denoted by k_{center}.**

from $\widetilde{\mathbf{h}}^{(\mathrm{b})}[n]$ into a single matrix $\widetilde{\mathbf{H}}^{(\mathrm{b})} \in \mathbb{C}^{M_{\mathrm{Tx}}^{(\mathrm{b})} \times N^{(\mathrm{b})}}$. Prior to the angular spectrum calculation, we estimate the sample covariance matrix as [84]

$$\widetilde{\mathbf{C}}^{(\mathrm{b})} = \frac{1}{N^{(\mathrm{b})}} \widetilde{\mathbf{H}}^{(\mathrm{b})} \left(\widetilde{\mathbf{H}}^{(\mathrm{b})}\right)^{\mathrm{H}}. \tag{31}$$

The angular power spectrum of the Bartlett beamformer is obtained by computing

$$P_{\vartheta}^{(\mathrm{b})}\left(\vartheta_{\mathrm{tr}}\right) = \frac{\left(\mathbf{a}_{\mathrm{Tx}}^{(\mathrm{b})}\left(\vartheta_{\mathrm{tr}}\right)\right)^{\mathrm{H}} \widetilde{\mathbf{C}}^{(\mathrm{b})}\, \mathbf{a}_{\mathrm{Tx}}^{(\mathrm{b})}\left(\vartheta_{\mathrm{tr}}\right)}{\left(\mathbf{a}_{\mathrm{Tx}}^{(\mathrm{b})}\left(\vartheta_{\mathrm{tr}}\right)\right)^{\mathrm{H}} \mathbf{a}_{\mathrm{Tx}}^{(\mathrm{b})}\left(\vartheta_{\mathrm{tr}}\right)}, \tag{32}$$

where

$$\mathbf{a}_{\mathrm{Tx}}^{(\mathrm{b})}\left(\vartheta_{\mathrm{tr}}\right) = e^{-\mathrm{j}2\pi \frac{r_{\mathrm{m}}^{(\mathrm{b})}}{\lambda^{(\mathrm{b})}} \sin(\vartheta_{\mathrm{tr}}) \sin\left(\boldsymbol{\varphi}_{\mathrm{com}}^{(\mathrm{b})}\right)} \tag{33}$$

represents the steering vector for the trial angle-of-departure (AoD) ϑ_{tr}. The trial angle ϑ_{tr} can take $L_{\vartheta_{\mathrm{tr}}}$ potential angles within the range of $[-90°, 90°]$. In (33), $r_{\mathrm{m}}^{(\mathrm{b})} = 1$ denotes the radius of the rotary unit, while

$$\boldsymbol{\varphi}_{\mathrm{com}}^{(\mathrm{b})} = \frac{\Delta d^{(\mathrm{b})}}{r_{\mathrm{m}}^{(\mathrm{b})}} \left[-\tfrac{M_{\mathrm{Tx}}^{(\mathrm{b})}-1}{2} \quad -\tfrac{M_{\mathrm{Tx}}^{(\mathrm{b})}-1}{2}+1 \quad \cdots \quad \tfrac{M_{\mathrm{Tx}}^{(\mathrm{b})}-1}{2}\right]^{\mathrm{T}} \tag{34}$$

represents a compensation angle introduced to compensate for slight mismatches in the antenna positions within the elevation plane. This adjustment ensures that the antenna positions precisely follow the arc in the elevation plane, as illustrated in Fig. 8. The normalized angular power spectrum for the spatial position $(\mathrm{x}, \mathrm{y}) = (1, 12)$, located within the corresponding environment, is shown in Fig. 9. It can be observed that the angular power spectra are similar across different frequency bands. Furthermore, the spectra are largely invariant with respect to the transmitter velocity, as indicated by the similar patterns between scenarios A and B (sub-6 GHz) and between scenarios C and D (mmWave). In this specific case, we observe that the majority of the power for both frequency bands is concentrated around the 0°, corresponding to the direction of the receive antenna, which suggests that the main signal component passes through wall A. Additionally, the first side lobes for both sub-6 GHz and mmWave scenarios are approximately 7 dB weaker than the main lobe. The angular power is dominantly concentrated

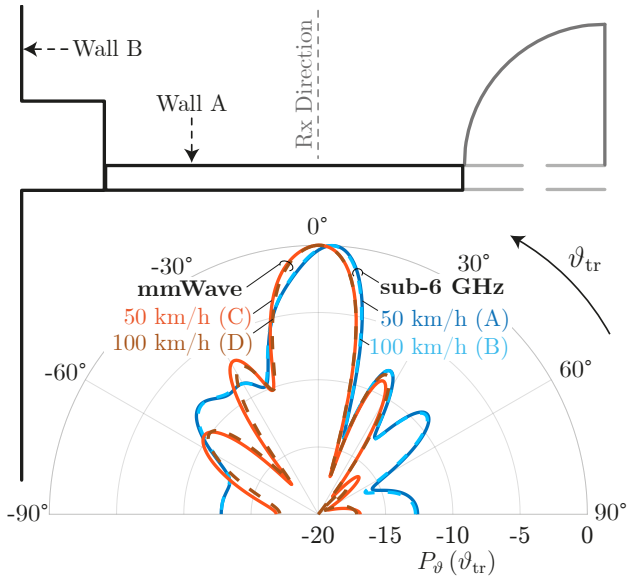

FIGURE 9. **The angular power spectra are similar across different frequency bands, with the majority of the power concentrated around 0°. Moreover, spectra are largely invariant with respect to the transmitter velocity.**

around the main lobe, with limited dispersion into off-axis directions. The pronounced attenuation of the side lobes reflects the directional nature of the received signal and emphasizes the impact of the spatial filtering introduced by the highly directive receive horn antennas.

Furthermore, we identify the N_{ϑ} highest peaks of $P_{\vartheta}^{(\mathrm{b})}\left(\vartheta_{\mathrm{tr}}\right)$ using a simple peak-finding algorithm. The angles at which these peaks occur correspond to the $N_{\vartheta} = 5$ strongest AoDs. In addition to extracting the AoDs, we calculate the RMS angular spread, an important parameter in multi-antenna systems that quantifies the degree of spatial selectivity [8]. The RMS angular spread is given by [85]

$$\sigma_{\vartheta}^{(\mathrm{b})} = \sqrt{\frac{\sum\limits_{\forall \vartheta_{\mathrm{tr}}} \left| e^{\mathrm{j}\vartheta_{\mathrm{tr}}} - \mu_{\vartheta}^{(\mathrm{b})} \right|^2 P_{\vartheta}^{(\mathrm{b})}\left(\vartheta_{\mathrm{tr}}\right)}{\sum\limits_{\forall \vartheta_{\mathrm{tr}}} P_{\vartheta}^{(\mathrm{b})}\left(\vartheta_{\mathrm{tr}}\right)}} \tag{35}$$

with

$$\mu_{\vartheta}^{(\mathrm{b})} = \frac{\sum\limits_{\forall \vartheta_{\mathrm{tr}}} e^{\mathrm{j}\vartheta_{\mathrm{tr}}} P_{\vartheta}^{(\mathrm{b})}\left(\vartheta_{\mathrm{tr}}\right)}{\sum\limits_{\forall \vartheta_{\mathrm{tr}}} P_{\vartheta}^{(\mathrm{b})}\left(\vartheta_{\mathrm{tr}}\right)}. \tag{36}$$

To statistically evaluate the spatial characteristics, we analyze the detected AoDs and the RMS angular spreads across all spatial positions. In Fig. 10, we plot a histogram of the N_{ϑ} strongest AoDs for each spatial location x and y. Furthermore, Fig. 11 illustrates the empirical CDF of the N_{ϑ} strongest AoDs (Fig. 11a) and the RMS angular spread $\sigma_{\vartheta}^{(\mathrm{b})}[\mathrm{x}, \mathrm{y}]$ (Fig. 11b), considering all spatial positions. The corresponding mean and standard deviation values for the different scenarios are summarized in Tab. 2.

It can be observed that both the sub-6 GHz and mmWave bands exhibit AoD values predominantly spread between

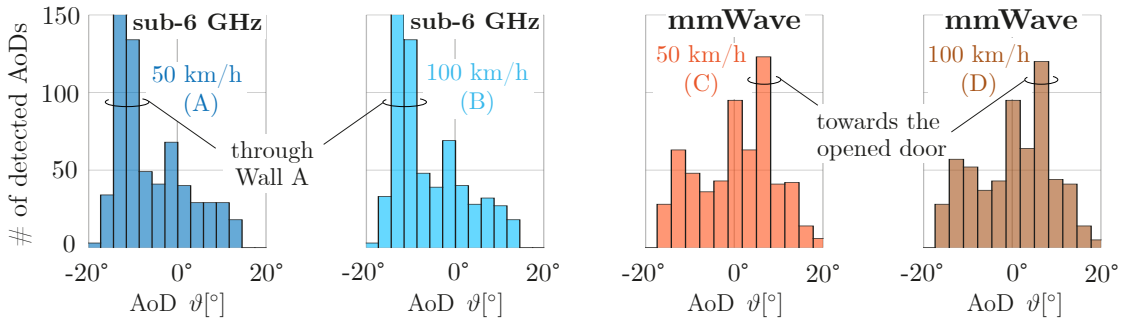

FIGURE 10. For both bands, most power is concentrated around 0°, matching the main receive antenna direction. In sub-6 GHz, more AoDs appear on the negative side (through wall A), while in mmWave, more AoDs occur on the positive side (towards the opened door).

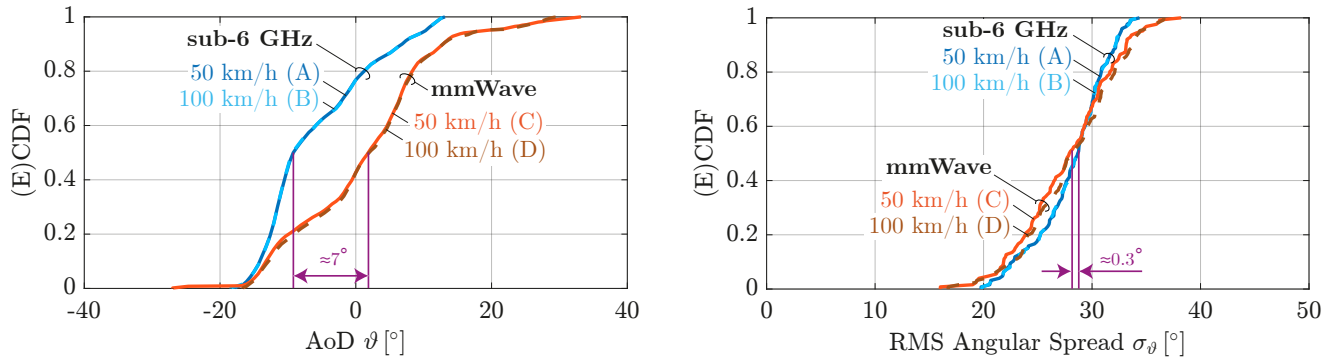

FIGURE 11. The sub-6 GHz and mmWave bands exhibit AoD values predominantly spread between approximately −20° to 20°, with very similar values of RMS angular spread.

approximately −20° to 20°. As already indicated in Fig. 9, the majority of the power for both frequency bands is concentrated around 0°, consistent with the main direction of the receive antenna. Nevertheless, some differences between the frequency bands are apparent. In the sub-6 GHz band, more detected AoDs are located on the negative side (from −20° to 0°), corresponding to propagation through wall A. In contrast, in the mmWave band, more detected AoDs are found on the positive side (from 0° to 20°), towards the opened door. Additionally, at mmWave frequencies, the mean AoD is approximately 7° larger than in the sub-6 GHz band. The standard deviation values of the AoDs are around 7.9° for the sub-6 GHz band and around 10° for the mmWave band. Regarding the RMS angular spread, both bands exhibit very similar mean values, around 28°, with only a difference of 0.3° between them. However, the mmWave bands show slightly higher deviation, with standard deviation values of 4.3° compared to 3.3° for the sub-6 GHz band. These results indicate that, despite the different propagation characteristics at sub-6 GHz and mmWave frequencies, the overall spatial characteristics — in terms of AoD distributions and angular spread — remain remarkably similar, with certain differences reflecting the influence of the propagation environment at different frequencies.

E. Comparison with Existing Literature

We compare our measured results for the RMS delay spread and RMS angular spread with values reported in prior studies, as well as with the reference values provided by the 3rd Generation Partnership Project (3GPP) [86]. To ensure a fair comparison, we restrict our focus to measurement campaigns conducted at comparable carrier frequencies and within similar indoor environments. We further differentiate between two propagation scenarios: LOS, where an unobstructed path exists between transmitter and receiver, and NLOS, where an obstacle such as a wall obstructs the direct path. Moreover, we limit the comparison to studies that report both RMS delay and azimuth angular spreads, in line with our analysis. The comparative results are summarized in Tab. 3, where we present the mean and standard deviation of both metrics across studies. For each reference, we include the carrier frequency, measurement setup type (e.g., antenna array (AA), rotating horn, or VAA)) and the antenna types used (e.g., omnidirectional, horn, log-periodic, or patch) at both the transmitter and receiver.

First, we observe that the mean RMS delay and angular spreads show comparable values across both sub-6 GHz and mmWave frequency bands, as well as across both LOS and NLOS propagation scenarios. Furthermore, the mean RMS delay and angular spreads observed in our measurements are consistent with values reported in the literature, across

TABLE 3. Overview of Existing RMS Delay Spread and Angular Spread Results in the Literature

		Frequency	Setup	Antenna Type		Parameter				Reference
		f_c [GHz]		Transmitter	Receiver	σ_τ [ns]		σ_ϑ [°]		
						Mean	Std.	Mean	Std.	
sub-6 GHz	LOS	2.5	VAA	Omni	Omni	20	N/A	23.96	N/A	A. Poon *et al.* [33]
		3	VAA	Omni	Omni	20	N/A	20.01	N/A	A. Poon *et al.* [33]
		2.4	Rotating	Horn	Horn	5.67	N/A	46.08	N/A	Y. L. C. De Jong *et al.* [61]
		2.55	N/A	Omni	Omni	20.06	1.51	47.47	1.53	3GPP [86]
	NLOS	**2.55**	**VAA**	**Horn**	**Omni**	**14.02**	**1.12**	**28.10**	**3.33**	**Our work**
		3.6	VAA	Log-Periodic	Omni	8.43	N/A	43.26	N/A	F. Quitin *et al.* [36]
		2.5	VAA	Omni	Omni	20	N/A	24.64	N/A	A. Poon *et al.* [33]
		3	VAA	Omni	Omni	20	N/A	24.51	N/A	A. Poon *et al.* [33]
		2.4	Rotating	Horn	Horn	14.25	N/A	38.41	N/A	Y. L. C. De Jong *et al.* [61]
		2.6	AA	Patch	Patch	33.56	N/A	27.50	N/A	C. Fang *et al.* [39]
		2.55	N/A	Omni	Omni	47.09	1.28	63.45	1.33	3GPP [86]
mmWave	LOS	26	Rotating	Horn	Horn	5.82	N/A	45.61	N/A	Y. L. C. De Jong *et al.* [61]
		28	Rotating	Horn	Horn	10.80	N/A	39.10	N/A	S. Ju *et al.* [55]
		28	VAA	Omni	Omni	13.6	N/A	39	N/A	A. Mudonhi *et al.* [49]
		25.5	Rotating	Horn	Horn	16.48	1.35	16.40	1.20	P. Zhang *et al.* [50]
		28	Rotating	Omni	Omni	12.45	N/A	32.48	N/A	G. Zhang *et al.* [51]
		28	Rotating	Horn	Horn	12.58	1.31	14.12	1.94	P. Tang *et al.* [56]
		25.5	N/A	Omni	Omni	19.66	1.51	32.40	1.94	3GPP [86]
	NLOS	**25.5**	**VAA**	**Horn**	**Omni**	**15.50**	**1.13**	**27.79**	**4.32**	**Our work**
		26	Rotating	Horn	Horn	16.18	N/A	25.90	N/A	Y. L. C. De Jong *et al.* [61]
		28	Rotating	Horn	Horn	17	N/A	31.80	N/A	S. Ju *et al.* [55]
		28	Rotating	Horn	Horn	18.91	N/A	32.16	N/A	J. Ko *et al.* [52]
		28	Rotating	Horn	Horn	23.98	1.44	17.37	1.90	P. Tang *et al.* [56]
		25.5	N/A	Omni	Omni	26.82	1.57	50.86	1.69	3GPP [86]

both sub-6 GHz and mmWave frequency bands. Notably, the measured mean values for the most reported measurements - particularly for the NLOS scenarios - are significantly lower than the corresponding values specified in the 3GPP indoor channel models.

Given the higher path loss and consequently lower SINR observed at mmWave frequencies compared to sub-6 GHz, it is essential to employ larger antenna arrays at both the transmitter and receiver to ensure sufficient link margins. Moreover, since the channel characteristics in the delay domain do not differ significantly across frequency bands, both sub-6 GHz and mmWave systems may employ comparable cyclic prefix lengths to effectively mitigate intersymbol interference. Furthermore, as Doppler effects and channel aging are significantly more pronounced at mmWave frequencies, these systems should utilize larger subcarrier spacing (i.e., shorter symbol durations) than sub-6 GHz systems to improve robustness against severe Doppler shifts.

IV. Performance Evaluation

In this section, we perform a comparative evaluation of the measured time-varying channels in the sub-6 GHz and mmWave bands in terms of the achievable SE for different multiple-input single-output (MISO) configurations. Following the approach in (28), the time-varying channel is constructed by approximating a uniform linear VAA in the azimuth plane over multiple time snapshots, given by

$$\widetilde{\mathbf{h}}^{(\mathrm{b})}\left[n,k'\right]=\widetilde{\mathrm{H}}_{w}^{(\mathrm{b})}\left[n,k'+\Delta k_{\mathrm{snap}}^{(\mathrm{b})}\mathbf{d}^{(\mathrm{b})}\right]\in\mathbb{C}^{1\times M_{\mathrm{Tx}}^{(\mathrm{b})}}. \quad (37)$$

The antenna element positions are denoted by $\mathbf{d}^{(\mathrm{b})}$, as defined in (29) and

$$k'\in\left\{-\frac{K_{\mathrm{eval}}^{(\mathrm{b})}-1}{2},\ldots,\frac{K_{\mathrm{eval}}^{(\mathrm{b})}-1}{2}\right\} \quad (38)$$

indexes the time snapshots. For performance evaluation, we consider $K_{\mathrm{eval}}^{(\mathrm{b})}$ time snapshots. During the training phase, only one snapshot is utilized for calculating the precoder, which is denoted by k'_{T}, while the remaining $K_{\mathrm{eval}}^{(\mathrm{b})}-1$

TABLE 4. Parameters Used for Performance Evaluation

Parameter	Value	
Frequency Band	sub-6 GHz	mmWave
Carrier Frequency f_c	2.55 GHz	25.5 GHz
Evaluation Snapshots K_{eval}	7	7
Bandwidth B	100 MHz	100 MHz
Snapshot Spacing Δk_{snap}	20	2
Number of Transmit Antennas M_{Tx}	{2, 4, 8, 12}	{2, 4, 8, 12}

snapshots are used for data transmission. In what follows, we set $k'_{\text{T}} = -\frac{K^{(\text{b})}_{\text{eval}}-1}{2}$ and therefore the channel at the training snapshot is given by

$$\overline{\mathbf{h}}^{(\text{b})}[n] = \widetilde{\mathbf{h}}^{(\text{b})}[n, k'_{\text{T}}]. \tag{39}$$

To achieve the highest performance in terms of SE, we compute the precoding vector $\overline{\mathbf{f}}^{(\text{b})}[n] \in \mathbb{C}^{M^{(\text{b})}_{\text{Tx}} \times 1}$ using a matched filter, given by

$$\overline{\mathbf{f}}^{(\text{b})}[n] = \left(\overline{\mathbf{h}}^{(\text{b})}[n]\right)^{\text{H}}. \tag{40}$$

For ideal precoding, $\widetilde{\mathbf{f}}^{(\text{b})}[n, k']$ is computed as a matched filter for each snapshot k', i.e.,

$$\widetilde{\mathbf{f}}^{(\text{b})}[n, k'] = \left(\widetilde{\mathbf{h}}^{(\text{b})}[n, k']\right)^{\text{H}}. \tag{41}$$

Further, we ensure that the total transmit power constraints $\left\|\overline{\mathbf{f}}^{(\text{b})}[n]\right\|^2 = P^{(\text{b})}_{\text{T}}$ and $\left\|\widetilde{\mathbf{f}}^{(\text{b})}[n, k']\right\|^2 = P^{(\text{b})}_{\text{T}}$ are satisfied by the precoders for all subcarriers and snapshots. Since we consider MISO configurations with only a single receive antenna, transmission is limited to a single spatial stream. The achievable SE, expressed in bits/s/Hz and averaged over $N^{(\text{b})}$ subcarriers and $K^{(\text{b})}_{\text{eval}} - 1$ snapshots is given by

$$\text{SE}^{(\text{b})} = \frac{\sum_{\forall n} \sum_{\substack{\forall k' \\ k' \neq k'_{\text{T}}}} \log_2\left(1 + \text{SINR}^{(\text{b})}[n, k']\right)}{N^{(\text{b})}\left(K^{(\text{b})}_{\text{eval}} - 1\right)}. \tag{42}$$

The corresponding effective SINR for the MISO case is denoted by

$$\text{SINR}^{(\text{b})}[n, k'] = \frac{\left|\widetilde{\mathbf{h}}^{(\text{b})}[n, k']\,\overline{\mathbf{f}}^{(\text{b})}[n]\right|^2}{\overline{\sigma}^2_{wI^{(\text{b})}}}. \tag{43}$$

In (43), $\overline{\sigma}^2_{wI^{(\text{b})}}$ denotes the power of the noise plus interference, averaged over considered snapshots, i.e.,

$$\overline{\sigma}^2_{wI^{(\text{b})}} = \frac{1}{K^{(\text{b})}_{\text{eval}}} \sum_{\forall k'} \widetilde{\sigma}^2_{wI^{(\text{b})}}[k']. \tag{44}$$

In Fig. 12, we plot the achievable SE as a function of the number of transmit antennas. The SE values are averaged over spatial positions, with the evaluation parameters summarized in Tab. 4. Besides scenarios with imperfect precoding $\overline{\mathbf{f}}^{(\text{b})}[n]$, we also consider perfect CSI cases employing the perfect precoder $\widetilde{\mathbf{f}}^{(\text{b})}[n, k']$ for each considered snapshot.

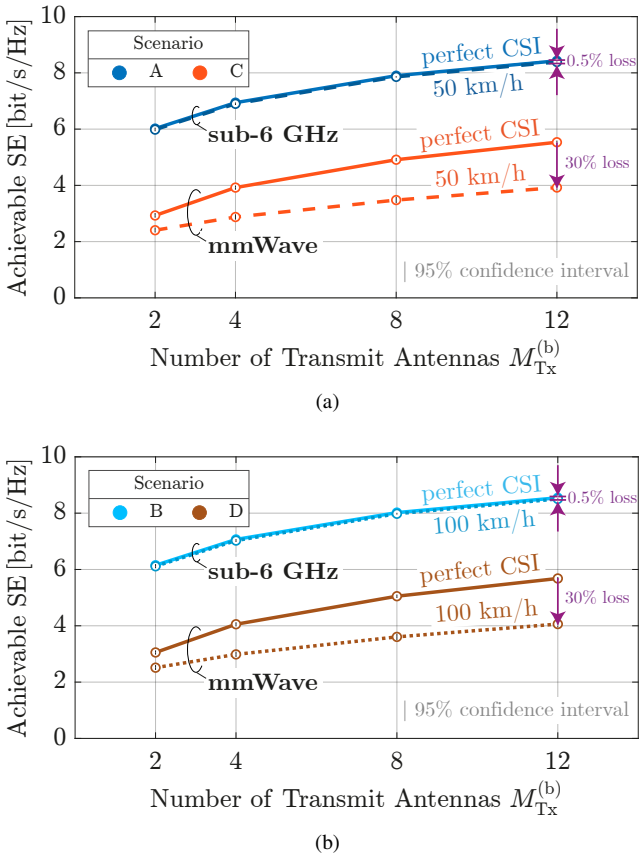

FIGURE 12. The performance gap in SE between ideal precoding (perfect CSI) and imperfect precoding (50 km/h or 100 km/h) is significantly larger in the mmWave band - 1.6 bit/s/Hz (30%) - than in the sub-6 GHz band, where it is only 0.04 bit/s/Hz (0.5%).

Using the perfect precoder $\widetilde{\mathbf{f}}^{(\text{b})}[n, k']$ eliminates the impact of antenna movement and establishes an upper bound on SE performance.

As expected, the sub-6 GHz band achieves higher achievable SE than the mmWave band. This is primarily due to a higher estimated SINR, with $\widetilde{\gamma}^{(\text{s})}_{wI}[k] \approx 22$ dB at sub-6 GHz, compared to $\widetilde{\gamma}^{(\text{m})}_{wI}[k] \approx 11$ dB at mmWave. Additionally, the achievable SE increases with the number of transmit antennas, regardless of the frequency band. Under perfect CSI conditions (ideal precoder per snapshot), both bands show a similar gain of approximately 2.5 bit/s/Hz when increasing antennas from 2 to 12. However, with imperfect precoding, the sub-6 GHz band achieves a significantly higher gain of approximately 2.5 bit/s/Hz compared to the mmWave band, which gains only about 1.5 bit/s/Hz. In particular, in the sub-6 GHz band for $M^{(\text{b})}_{\text{Tx}} = 12$, imperfect precoding leads to an SE loss of only 0.04 bit/s/Hz (0.5%) compared to the perfect CSI case. In contrast, in the mmWave band, the loss increases substantially to 1.6 bit/s/Hz (30%). This higher performance loss in the mmWave SE is attributed to more pronounced channel variations caused by transmit antenna movement, which impact mmWave channels more significantly than those at sub-6 GHz.

The SE performance at the lower velocity of 50 km/h (Fig. 12a) coincides with that at the higher velocity of 100 km/h (Fig. 12b), for both ideal and imperfect precoding. This behavior can be explained by the shorter symbol duration at 100 km/h, which is exactly half that at 50 km/h (see Tab. 1). As a result, the impact of the higher velocity is effectively compensated and no additional performance loss is observed when increasing the velocity.

Note that the presented performance evaluation does not include channel prediction. However, the SE performance under imperfect precoding could potentially be improved by applying existing channel prediction and tracking methods [87]–[89].

V. Conclusion

In this paper, we present dynamic multi-band wireless channel measurements conducted in an indoor environment, enabling a direct comparison of propagation characteristics at sub-6 GHz and mmWave bands. The normalized LSFs at both sub-6 GHz and mmWave bands exhibit similar overall characteristics, with the majority of the channel power concentrated within delay values of approximately 20-80 ns and normalized Doppler shifts between -3 and 4 ns/m. However, the mmWave LSF reveals more distinct multipath components and the channel power at mmWave frequencies decays more rapidly with increasing delay and Doppler shift compared to sub-6 GHz.

Furthermore, the delay-domain analysis shows that the sub-6 GHz and mmWave channels exhibit similar values of RMS delay spread and Rician K-factor, indicating comparable propagation conditions at sub-6 GHz and mmWave frequencies. In the Doppler domain, the RMS Doppler spread scales proportionally with the carrier frequency and the corresponding transmitter's velocity, as expected. However, the normalized RMS Doppler spread values remain comparable across the frequency bands. In the angular domain, both sub-6 GHz and mmWave channels show similar AoD distributions, primarily concentrated between approximately -20° and 20°, with RMS angular spread values around 30°. This indicates that the spatial characteristics of the channel are remarkably similar at both frequency bands. Moreover, the observed values of RMS delay spread, Rician K-factor, normalized RMS Doppler spread and RMS angular spread are almost invariant with regard to the transmitter's velocity, despite measurements being conducted at different times. This consistency highlights the high accuracy and repeatability of the proposed measurement setup, capable of reproducing experiments with minimal uncertainty. Finally, the measured values of RMS delay spread and RMS angular spread are in good agreement with previously reported results in the literature for both sub-6 GHz and mmWave frequencies.

The sub-6 GHz band achieves a higher achievable SE compared to the mmWave band, primarily due to its higher estimated SINR. At mmWave frequencies, however, CSI becomes outdated rapidly due to increased Doppler shifts caused by transmitter movement which significantly degrades system performance. In summary, differences in delay-domain parameters such as RMS delay spread and Rician K-factor, as well as angular-domain parameters like RMS angular spread, are minor at the system level and are unlikely to have a significant impact on overall system design. In contrast, the RMS Doppler spread scales proportionally with carrier frequency and transmitter velocity, resulting in significantly faster CSI aging at mmWave frequencies. This sensitivity to mobility poses a substantial limitation for mmWave systems in dynamic scenarios.

REFERENCES

[1] F. Pasic, M. Hofer, M. Mussbah, H. Groll, T. Zemen, S. Schwarz, and C. F. Mecklenbräuker, "Statistical evaluation of delay and Doppler spreads in sub-6 GHz and mmWave vehicular channels," in *2023 IEEE 97th Vehicular Technology Conference (VTC2023-Spring)*, 2023.

[2] P. Jonsson, "Ericsson mobility report," Ericsson, Stockholm, Sweden, Technical Report EAB-24:009018 Uen Rev C, 2024, https://www.ericsson.com/4adb7e/assets/local/reports-papers/mobility-report/documents/2024/ericsson-mobility-report-november-2024.pdf.

[3] O. Kanhere, H. Poddar, and T. S. Rappaport, "Calibration of NYURay for ray tracing using 28, 73, and 142 GHz channel measurements conducted in indoor, outdoor, and factory scenarios," *IEEE Transactions on Antennas and Propagation*, vol. 73, no. 1, pp. 405–420, 2025.

[4] 3GPP, "Technical Specification Group Radio Access Network; NR; User Equipment (UE) radio transmission and reception; Part 1: Range 1 Standalone," 3rd Generation Partnership Project (3GPP), Technical Specification (TS) 38.101-1, 2022, version 17.5.0.

[5] T. S. Rappaport, S. Sun, R. Mayzus, H. Zhao, Y. Azar, K. Wang, G. N. Wong, J. K. Schulz, M. Samimi, and F. Gutierrez, "Millimeter wave mobile communications for 5G cellular: It will work!" *IEEE Access*, vol. 1, pp. 335–349, 2013.

[6] F. Pasic, N. Di Cicco, M. Skocaj, M. Tornatore, S. Schwarz, C. F. Mecklenbräuker, and V. Degli-Esposti, "Multi-band measurements for deep learning-based dynamic channel prediction and simulation," *IEEE Communications Magazine*, vol. 61, no. 9, pp. 98–104, 2023.

[7] A. F. Molisch, C. F. Mecklenbräuker, T. Zemen, A. Prokes, M. Hofer, F. Pasic, and H. Hammoud, "Millimeter-wave V2X channel measurements in urban environments," *IEEE Open Journal of Vehicular Technology*, vol. 6, pp. 520–541, 2025.

[8] A. F. Molisch, *Wireless communications: From Fundamentals to Beyond 5G*, 3rd ed. IEEE Press - Wiley, 2023.

[9] T. S. Rappaport, G. R. MacCartney, S. Sun, H. Yan, and S. Deng, "Small-scale, local area, and transitional millimeter wave propagation for 5G communications," *IEEE Transactions on Antennas and Propagation*, vol. 65, no. 12, pp. 6474–6490, 2017.

[10] M. Shafi, H. Tataria, A. F. Molisch, F. Tufvesson, and G. Tunnicliffe, "Real-time deployment aspects of C-band and millimeter-wave 5G-NR systems," in *ICC 2020 - 2020 IEEE International Conference on Communications (ICC)*, 2020.

[11] A. Ali, N. Gonzalez-Prelcic, R. W. Heath, and A. Ghosh, "Leveraging sensing at the infrastructure for mmWave communication," *IEEE Communications Magazine*, vol. 58, no. 7, pp. 84–89, 2020.

[12] F. Pasic, M. Hofer, M. Mussbah, S. Sangodoyin, S. Caban, S. Schwarz, T. Zemen, M. Rupp, A. F. Molisch, and C. F. Mecklenbräuker, "Millimeter wave MIMO channel estimation using sub-6 GHz out-of-band information," *IEEE Transactions on Communications*, 2025.

[13] F. Pasic, M. Hofer, M. Mussbah, S. Caban, S. Schwarz, T. Zemen, and C. F. Mecklenbräuker, "Channel estimation for mmWave MIMO using sub-6 GHz out-of-band information," in *2024 International Conference on Smart Applications, Communications and Networking (SmartNets)*, 2024.

[14] M. Hofer, F. Pasic, B. Rainer, J. Blumenstein, A. Prokes, C. F. Mecklenbräuker, A. F. Molisch, and T. Zemen, "Enabling vehicular mmWave communication links using cmWave information," in *2025 19th European Conference on Antennas and Propagation (EuCAP)*, 2025.

[15] F. Pasic, L. Eller, S. Schwarz, M. Rupp, and C. F. Mecklenbräuker, "Deep learning-based mmWave MIMO channel estimation using sub-6 GHz channel information: CNN and UNet approaches," *IEEE INFOCOM 2025 - IEEE Conference on Computer Communications Workshops (INFOCOM WKSHPS)*, 2025, presented. [Online]. Available: https://owncloud.tuwien.ac.at/index.php/s/828AQoql3xLSIxs

[16] S. Sangodoyin, U. T. Virk, D. Burghal, K. Haneda, and A. F. Molisch, "Joint characterization of mm-wave and cm-wave device-to-device fading channels," in *MILCOM 2018 - 2018 IEEE Military Communications Conference (MILCOM)*, 2018, pp. 194–200.

[17] H. Miao, J. Zhang, P. Tang, L. Tian, X. Zhao, B. Guo, and G. Liu, "Sub-6 GHz to mmWave for 5G-advanced and beyond: Channel measurements, characteristics and impact on system performance," *IEEE Journal on Selected Areas in Communications*, vol. 41, no. 6, pp. 1945–1960, 2023.

[18] D. Dupleich, R. Muller, C. Schneider, S. Skoblikov, J. Luo, M. Boban, G. Del Galdo, and R. Thoma, "Multi-band vehicle to vehicle channel measurements from 6 GHz to 60 GHz at "T" intersection," in *2nd Connected and Automated Vehicles Symposium (CAVS)*, 2019.

[19] M. Boban, D. Dupleich, N. Iqbal, J. Luo, C. Schneider, R. Müller, Z. Yu, D. Steer, T. Jämsä, J. Li, and R. S. Thomä, "Multi-band vehicle-to-vehicle channel characterization in the presence of vehicle blockage," *IEEE Access*, vol. 7, pp. 9724–9735, 2019.

[20] M. Hofer, D. Löschenbrand, S. Zelenbaba, A. Dakić, B. Rainer, and T. Zemen, "Wireless 3GHz and 30 GHz vehicle-to-vehicle measurements in an urban street scenario," in *2022 IEEE 96th Vehicular Technology Conference (VTC2022-Fall)*, 2022.

[21] H. Wang, X. Yin, J. Rodríguez-Piñeiro, J. Lee, and M. Kim, "Shadowing and multipath-fading statistics at 2.4 GHz and 39 GHz in vehicle-to-vehicle scenarios," in *2020 14th European Conference on Antennas and Propagation (EuCAP)*, 2020.

[22] M. Hofer, D. Löschenbrand, J. Blumenstein, H. Groll, S. Zelenbaba, B. Rainer, L. Bernadó, J. Vychodil, T. Mikulasek, E. Zöchmann, S. Sangodoyin, H. Hammoud, B. Schrenk, R. Langwieser, S. Pratschner, A. Prokes, A. F. Molisch, C. F. Mecklenbräuker, and T. Zemen, "Wireless vehicular multiband measurements in centimeterwave and millimeterwave bands," in *IEEE 32nd Annual International Symposium on Personal, Indoor and Mobile Radio Communications (PIMRC)*, 2021.

[23] M. Hofer, D. Löschenbrand, F. Pasic, D. Radovic, B. Rainer, J. Blumenstein, C. F. Mecklenbräuker, S. Sangodoyin, H. Hammoud, G. Matz, A. F. Molisch, and T. Zemen, "Similarity of wireless multiband propagation in urban vehicular-to-infrastructure scenarios," in *2024 IEEE 35th International Symposium on Personal, Indoor and Mobile Radio Communications (PIMRC)*, 2024.

[24] F. Pasic, M. Hofer, T. Zemen, A. F. Molisch, and C. F. Mecklenbräuker, "Time-varying Rician K-factor in measured vehicular channels at cmWave and mmWave bands," in *2025 19th European Conference on Antennas and Propagation (EuCAP)*, 2025.

[25] P. Pagani, P. Laly, E. P. Simon, V. Picquet, R. D'Errico, and D. P. Gaillot, "Joint sub-6 GHz and mm-Wave V2I MIMO radio channel characterization," in *2025 19th European Conference on Antennas and Propagation (EuCAP)*, 2025.

[26] Z. Ying, T. Jiang, P. Tang, J. Zhang, and L. Tian, "Analysis of delay characteristics at 4.9 GHz and 28 GHz in an indoor industrial scenario," in *2020 14th European Conference on Antennas and Propagation (EuCAP)*, 2020.

[27] D. Dupleich, N. Han, A. Ebert, R. Müller, S. Ludwig, A. Artemenko, J. Eichinger, T. Geiss, G. Del Galdo, and R. Thomä, "From sub-6 GHz to mm-wave: Simultaneous multi-band characterization of propagation from measurements in industry scenarios," in *2022 16th European Conference on Antennas and Propagation (EuCAP)*, 2022.

[28] A. Saleh and R. Valenzuela, "A statistical model for indoor multipath propagation," *IEEE Journal on Selected Areas in Communications*, vol. 5, no. 2, pp. 128–137, 1987.

[29] T. Rappaport, "Characterization of UHF multipath radio channels in factory buildings," *IEEE Transactions on Antennas and Propagation*, vol. 37, no. 8, pp. 1058–1069, 1989.

[30] T. Rappaport, S. Seidel, and K. Takamizawa, "Statistical channel impulse response models for factory and open plan building radio communicate system design," *IEEE Transactions on Communications*, vol. 39, no. 5, pp. 794–807, 1991.

[31] C. Ho and T. Rappaport, "Effects of antenna polarization and beam pattern on multipath delay spread and path loss in indoor obstructed wireless channels," in *1st International Conference on Universal Personal Communications - ICUPC '92 Proceedings*, 1992, pp. 04.02/1–04.02/5.

[32] G. Janssen, P. Stigter, and R. Prasad, "Wideband indoor channel measurements and BER analysis of frequency selective multipath channels at 2.4, 4.75, and 11.5 GHz," *IEEE Transactions on Communications*, vol. 44, no. 10, pp. 1272–1288, 1996.

[33] A. Poon and M. Ho, "Indoor multiple-antenna channel characterization from 2 to 8 GHz," in *IEEE International Conference on Communications, 2003. ICC '03.*, vol. 5, 2003, pp. 3519–3523 vol.5.

[34] S. Ghassemzadeh, R. Jana, C. Rice, W. Turin, and V. Tarokh, "Measurement and modeling of an ultra-wide bandwidth indoor channel," *IEEE Transactions on Communications*, vol. 52, no. 10, pp. 1786–1796, 2004.

[35] C. Oestges, D. Vanhoenacker-Janvier, and B. Clerckx, "Channel characterization of indoor wireless personal area networks," *IEEE Transactions on Antennas and Propagation*, vol. 54, no. 11, pp. 3143–3150, 2006.

[36] F. Quitin, C. Oestges, F. Horlin, and P. De Doncker, "Clustered channel characterization for indoor polarized MIMO systems," in *2009 IEEE 20th International Symposium on Personal, Indoor and Mobile Radio Communications*, 2009, pp. 1064–1068.

[37] G. Durgin, V. Kukshya, and T. Rappaport, "Wideband measurements of angle and delay dispersion for outdoor and indoor peer-to-peer radio channels at 1920 MHz," *IEEE Transactions on Antennas and Propagation*, vol. 51, no. 5, pp. 936–944, 2003.

[38] F. Mani, F. Quitin, and C. Oestges, "Directional spreads of dense multipath components in indoor environments: Experimental validation of a ray-tracing approach," *IEEE Transactions on Antennas and Propagation*, vol. 60, no. 7, pp. 3389–3396, 2012.

[39] C. Fang, B. Allen, E. Liu, P. Karadimas, J. Zhang, A. A. Glazunov, and F. Tufvesson, "Indoor-indoor and indoor-outdoor propagation trial results at 2.6 GHz," in *2012 Loughborough Antennas & Propagation Conference (LAPC)*, 2012.

[40] Q. Wei, P. Tang, H. Miao, W. Zuo, L. Tian, J. Zhang, G. Liu, and M. Jian, "Measurement-based analysis of XL-MIMO channel characteristics in a corridor scenario," in *2024 IEEE 99th Vehicular Technology Conference (VTC2024-Spring)*, 2024.

[41] H. Xu, V. Kukshya, and T. Rappaport, "Spatial and temporal characteristics of 60-GHz indoor channels," *IEEE Journal on Selected Areas in Communications*, vol. 20, no. 3, pp. 620–630, 2002.

[42] S. Geng, J. Kivinen, X. Zhao, and P. Vainikainen, "Millimeter-wave propagation channel characterization for short-range wireless communications," *IEEE Transactions on Vehicular Technology*, vol. 58, no. 1, pp. 3–13, 2009.

[43] X. Wu, C.-X. Wang, J. Sun, J. Huang, R. Feng, Y. Yang, and X. Ge, "60-GHz millimeter-wave channel measurements and modeling for indoor office environments," *IEEE Transactions on Antennas and Propagation*, vol. 65, no. 4, pp. 1912–1924, 2017.

[44] T. Manabe, Y. Miura, and T. Ihara, "Effects of antenna directivity and polarization on indoor multipath propagation characteristics at 60 GHz," *IEEE Journal on Selected Areas in Communications*, vol. 14, no. 3, pp. 441–448, 1996.

[45] K. Sato, T. Manabe, T. Ihara, H. Saito, S. Ito, T. Tanaka, K. Sugai, N. Ohmi, Y. Murakami, M. Shibayama, Y. Konishi, and T. Kimura, "Measurements of reflection and transmission characteristics of interior structures of office building in the 60-GHz band," *IEEE Transactions on Antennas and Propagation*, vol. 45, no. 12, pp. 1783–1792, 1997.

[46] T. Zwick, T. Beukema, and H. Nam, "Wideband channel sounder with measurements and model for the 60 GHz indoor radio channel," *IEEE Transactions on Vehicular Technology*, vol. 54, no. 4, pp. 1266–1277, 2005.

[47] E. Zöchmann, M. Lerch, S. Caban, C. Mecklenbräuker, C. Mecklenbrauker, and M. Rupp, "Directional evaluation of receive power, Rician K-factor and RMS delay spread obtained from power measurements of 60 GHz indoor channels," in *2016 IEEE-APS Topical Conference on Antennas and Propagation in Wireless Communications (APWC)*, 2016, pp. 246–249.

[48] A. Mudonhi, R. D'Errico, and C. Oestges, "Indoor mmWave channel characterization with large virtual antenna arrays," in *2020 14th European Conference on Antennas and Propagation (EuCAP)*, 2020.

[49] ——, "Analysis of multipath components distributions over a large array in indoor mmWave channels," *IEEE Transactions on Antennas and Propagation*, vol. 70, no. 9, pp. 8330–8336, 2022.

[50] P. Zhang, J. Li, H. Wang, H. Wang, and W. Hong, "Indoor small-scale spatiotemporal propagation characteristics at multiple millimeter-wave bands," *IEEE Antennas and Wireless Propagation Letters*, vol. 17, no. 12, pp. 2250–2254, 2018.

[51] G. Zhang, K. Saito, W. Fan, X. Cai, P. Hanpinitsak, J.-I. Takada, and G. F. Pedersen, "Experimental characterization of millimeter-wave indoor propagation channels at 28 GHz," *IEEE Access*, vol. 6, pp. 76 516–76 526, 2018.

[52] J. Ko, Y.-J. Cho, S. Hur, T. Kim, J. Park, A. F. Molisch, K. Haneda, M. Peter, D.-J. Park, and D.-H. Cho, "Millimeter-wave channel measurements and analysis for statistical spatial channel model in in-building and urban environments at 28 GHz," *IEEE Transactions on Wireless Communications*, vol. 16, no. 9, pp. 5853–5868, 2017.

[53] G. R. Maccartney, T. S. Rappaport, S. Sun, and S. Deng, "Indoor office wideband millimeter-wave propagation measurements and channel models at 28 and 73 GHz for ultra-dense 5G wireless networks," *IEEE Access*, vol. 3, pp. 2388–2424, 2015.

[54] Y. Xing, T. S. Rappaport, and A. Ghosh, "Millimeter wave and sub-THz indoor radio propagation channel measurements, models, and comparisons in an office environment," *IEEE Communications Letters*, vol. 25, no. 10, pp. 3151–3155, 2021.

[55] S. Ju, Y. Xing, O. Kanhere, and T. S. Rappaport, "Millimeter wave and sub-Terahertz spatial statistical channel model for an indoor office building," *IEEE Journal on Selected Areas in Communications*, vol. 39, no. 6, pp. 1561–1575, 2021.

[56] P. Tang, J. Zhang, M. Shafi, P. A. Dmochowski, and P. J. Smith, "Millimeter wave channel measurements and modelling in an indoor hotspot scenario at 28 GHz," in *2018 IEEE 88th Vehicular Technology Conference (VTC-Fall)*, 2018.

[57] C. Anderson and T. Rappaport, "In-building wideband partition loss measurements at 2.5 and 60 GHz," *IEEE Transactions on Wireless Communications*, vol. 3, no. 3, pp. 922–928, 2004.

[58] O. H. Koymen, A. Partyka, S. Subramanian, and J. Li, "Indoor mm-Wave channel measurements: Comparative study of 2.9 GHz and 29 GHz," in *2015 IEEE Global Communications Conference (GLOBECOM)*, 2015.

[59] U. T. Virk, S. L. H. Nguyen, and K. Haneda, "Multi-frequency power angular spectrum comparison for an indoor environment," in *2017 11th European Conference on Antennas and Propagation (EUCAP)*, 2017, pp. 3389–3393.

[60] S. L. H. Nguyen, J. Medbo, M. Peter, A. Karttunen, K. Haneda, A. Bamba, R. D'Errico, N. Iqbal, C. Diakhate, and J.-M. Conrat, "On the frequency dependency of radio channel's delay spread: Analyses and findings from mmMAGIC multi-frequency channel sounding," in *12th European Conference on Antennas and Propagation (EuCAP 2018)*, 2018.

[61] Y. L. C. De Jong, J. A. Pugh, M. Bennai, and P. Bouchard, "2.4 to 61 GHz multiband double-directional propagation measurements in indoor office environments," *IEEE Transactions on Antennas and Propagation*, vol. 66, no. 9, pp. 4806–4820, 2018.

[62] T. Jiang, J. Zhang, M. Shafi, L. Tian, and P. Tang, "The comparative study of S-V model between 3.5 and 28 GHz in indoor and outdoor scenarios," *IEEE Transactions on Vehicular Technology*, vol. 69, no. 3, pp. 2351–2364, 2020.

[63] G. Zhang, J. O. Nielsen, X. Cai, K. Saito, P. Hanpinitsak, J.-I. Takada, G. F. Pedersen, and W. Fan, "Modeling multi-frequency characteristics for classroom and hall scenarios at 2-4, 9-11 and 27-29 GHz bands," *IEEE Access*, vol. 9, pp. 14 549–14 563, 2021.

[64] F. Pasic, D. Schützenhöfer, E. Jirousek, R. Langwieser, H. Groll, S. Pratschner, S. Caban, S. Schwarz, and M. Rupp, "Comparison of sub 6 GHz and mmWave wireless channel measurements at high speeds," in *16th European Conference on Antennas and Propagation*, 2022.

[65] S. Caban, J. Rodas, and J. A. García-Naya, "A methodology for repeatable, off-line, closed-loop wireless communication system measurements at very high velocities of up to 560 km/h," in *2011 IEEE International Instrumentation and Measurement Technology Conference*, 2011.

[66] F. Pasic, S. Pratschner, R. Langwieser, and C. F. Mecklenbräuker, "High-mobility wireless channel measurements at 5.9 GHz in an urban environment," in *2022 International Balkan Conference on Communications and Networking (BalkanCom)*, 2022, pp. 100–104.

[67] F. Pasic, S. Pratschner, M. Rupp, and C. F. Mecklenbräukcr, "Pilot-aided channel estimation scheme for NR-V2X speed emulation technique," in *2022 56th Asilomar Conference on Signals, Systems, and Computers*, 2022, pp. 1202–1207.

[68] F. Pasic, M. Hofer, D. Radovic, H. Groll, S. Caban, T. Zemen, and C. F. Mecklenbräuker, "Quantifying the reproducibility of multi-band high speed wireless channel measurements," in *2023 IEEE 34th Annual International Symposium on Personal, Indoor and Mobile Radio Communications (PIMRC)*, 2023.

[69] F. Pasic, S. Pratschner, R. Langwieser, D. Schützenhöfer, E. Jirousek, H. Groll, S. Caban, and M. Rupp, "Sub 6 GHz versus mmWave measurements in a controlled high-mobility environment," in *WSA 2021; 25th International ITG Workshop on Smart Antennas*, 2021.

[70] B.-J. Choi, E.-L. Kuan, and L. Hanzo, "Crest-factor study of MC-CDMA and OFDM," in *50th Vehicular Technology Conference*, vol. 1, 1999.

[71] 3GPP, "NR; User Equipment (UE) radio transmission and reception; Part 2: Range 2 Standalone," 3rd Generation Partnership Project (3GPP), Technical Specification (TS) 38.101-2, 2018.

[72] E. Sousa, V. Jovanovic, and C. Daigneault, "Delay spread measurements for the digital cellular channel in Toronto," *IEEE Transactions on Vehicular Technology*, vol. 43, no. 4, pp. 837–847, 1994.

[73] D. Dupleich, R. Müller, and R. Thomä, "Practical aspects on the noise floor estimation and cut-off margin in channel sounding applications," in *2021 15th European Conference on Antennas and Propagation (EuCAP)*, 2021.

[74] L. Bernadó, T. Zemen, F. Tufvesson, A. F. Molisch, and C. F. Mecklenbräuker, "Delay and Doppler spreads of nonstationary vehicular channels for safety-relevant scenarios," *IEEE Transactions on Vehicular Technology*, vol. 63, no. 1, 2014.

[75] G. Matz, "Doubly underspread non-WSSUS channels: analysis and estimation of channel statistics," in *2003 4th IEEE Workshop on Signal Processing Advances in Wireless Communications - SPAWC 2003 (IEEE Cat. No.03EX689)*, 2003, pp. 190–194.

[76] D. Radovic, F. Pasic, M. Hofer, T. Zemen, and C. F. Mecklenbräuker, "Stationarity of multiband channels for OTFS-based intelligent transportation systems," in *2024 18th European Conference on Antennas and Propagation (EuCAP)*, 2024.

[77] D. Slepian, "Prolate spheroidal wave functions, fourier analysis, and uncertainty — v: the discrete case," *The Bell System Technical Journal*, vol. 57, no. 5, pp. 1371–1430, 1978.

[78] E. Zöchmann, M. Hofer, M. Lerch, S. Pratschner, L. Bernadó, J. Blumenstein, S. Caban, S. Sangodoyin, H. Groll, T. Zemen, A. Prokeš, M. Rupp, A. F. Molisch, and C. F. Mecklenbräuker, "Position-specific statistics of 60 GHz vehicular channels during overtaking," *IEEE Access*, vol. 7, pp. 14 216–14 232, 2019.

[79] A. F. Molisch and M. Steinbauer, "Condensed parameters for characterizing wideband mobile radio channels," *International Journal of Wireless Information Networks*, vol. 6, no. 3, pp. 133–154, 1999.

[80] B. Fleury, "An uncertainty relation for WSS processes and its application to WSSUS systems," *IEEE Transactions on Communications*, vol. 44, no. 12, pp. 1632–1634, 1996.

[81] C. Oestges, N. Czink, B. Bandemer, P. Castiglione, F. Kaltenberger, and A. J. Paulraj, "Experimental characterization and modeling of outdoor-to-indoor and indoor-to-indoor distributed channels," *IEEE Transactions on Vehicular Technology*, vol. 59, no. 5, pp. 2253–2265, 2010.

[82] L. Greenstein, D. Michelson, and V. Erceg, "Moment-method estimation of the Ricean K-factor," *IEEE Communications Letters*, vol. 3, no. 6, pp. 175–176, 1999.

[83] H. L. Van Trees, *Optimum array processing: Part IV of detection, estimation, and modulation theory*. John Wiley & Sons, 2002.

[84] H. Krim and M. Viberg, "Two decades of array signal processing research: the parametric approach," *IEEE Signal Processing Magazine*, vol. 13, no. 4, pp. 67–94, 1996.

[85] B. Fleury, "First- and second-order characterization of direction dispersion and space selectivity in the radio channel," *IEEE Transactions on Information Theory*, vol. 46, no. 6, pp. 2027–2044, 2000.

[86] 3GPP, "Study on channel model for frequencies from 0.5 to 100 GHz," 3rd Generation Partnership Project (3GPP), Technical report (TR) 38.901, 2022, version 17.0.0.

[87] H. Kim, S. Kim, H. Lee, C. Jang, Y. Choi, and J. Choi, "Massive MIMO channel prediction: Kalman filtering vs. machine learning," *IEEE Transactions on Communications*, vol. 69, no. 1, pp. 518–528, 2021.
[88] M. Alrabeiah and A. Alkhateeb, "Deep learning for mmWave beam and blockage prediction using sub-6 GHz channels," *IEEE Transactions on Communications*, vol. 68, no. 9, pp. 5504–5518, 2020.
[89] K. Vuckovic, M. B. Mashhadi, F. Hejazi, N. Rahnavard, and A. Alkhateeb, "PARAMOUNT: Toward generalizable deep learning for mmWave beam selection using sub-6 GHz channel measurements," *IEEE Transactions on Wireless Communications*, vol. 23, no. 5, pp. 5187–5202, 2024.

FARUK PASIC (Graduate Student Member, IEEE) received the B.Sc. degree in electrical engineering and the Dipl. Ing. degree (M.Sc. equivalent) in telecommunications from the University of Sarajevo, Bosnia and Herzegovina and TU Wien, Austria, in 2017 and 2021, respectively. He was a Visiting Researcher at the University of Southern California, Los Angeles, CA, USA, in 2024, and at the Department of Electrical and Information Technology, Lund University, Sweden, in 2025. His research interests include wireless channel measurements and modeling, channel estimation, mmWave technology, MIMO systems and out-of-band aided communication.

MARIAM MUSSBAH received the B.Sc. degree in electrical engineering and the Dipl. Ing. degree (M.Sc. equivalent) in telecommunications engineering from TU Wien, Austria, in 2016 and 2020, respectively. Her research interests include link-level simulations, massive MIMO and cell-free MIMO systems.

MARKUS HOFER (Member, IEEE) received the Dipl.-Ing. degree (Hons.) in telecommunications from Vienna University of Technology, Vienna, Austria, in 2013, and the Ph.D. degree in 2019. From 2013 to 2015, he was with the Signal and Information Processing Department, FTW Telecommunications Research Center Vienna, as a Researcher. He has been with the AIT—Austrian Institute of Technology, Vienna, since 2015, and is working as a Scientist with the Wireless Research Group. His research interests include 6G wireless communications, reflective intelligent surfaces, joint communication and sensing, mmWave and multi-band communications, time-variant channel measurements, modeling and real-time emulation, as well as software-defined radio rapid prototyping.

SEBASTIAN CABAN received the master's degree in business administration, and the master's and Ph.D. degrees in telecommunications from the Technical University of Vienna (TU Wien), Vienna, Austria. His current research interests include measurements in wireless communications.

STEFAN SCHWARZ (Senior Member, IEEE) received the Dr. techn. degree (Ph.D. equivalent) in telecommunications engineering from the Technical University (TU) Wien, Austria, in 2013. Since 2021, he has been an Associate Professor at the Institute of Telecommunications, TU Wien, where he leads the Research Unit on Wireless Communications. His research interests include wireless communications, signal processing, wireless channel modeling, machine learning, and game theory. He currently serves as an Associate Editor for IEEE Communications Letters.

THOMAS ZEMEN (S'03–M'05–SM'10) received the Dipl.-Ing. degree, the doctoral degree and the Venia Docendi (Habilitation) from Technische Universität Wien (TU Wien). He joined AIT Austrian Institute of Technology in 2014 and is Principal Scientist since 2021 leading the wireless research group. Previously, Thomas Zemen worked for Siemens AG Austria and the Telecommunication Research Center Vienna (FTW). Mr. Zemen has published five book chapters, 52 journal papers, more than 161 conference communications, and two patents. His research interests are sustainable 6G physical layer radio communication technologies for time-sensitive applications with a focus on distributed MIMO systems, reconfigurable intelligent surfaces, multi-band communications, joint communication and sensing, and site-specific radio channel models. Dr. Zemen is docent at the Vienna University of Technology, teaching advanced wireless communications.

MARKUS RUPP (Fellow, IEEE) received the Dipl.-Ing. degree from the University of Saarbrücken, Germany, in 1988, and the Dr.-Ing. degree from Technische Universität Darmstadt, Germany, in 1993. Until 1995, he had a postdoctoral position with the University of California, Santa Barbara. From 1995 to 2001, he was a member of the Technical Staff of the Wireless Technology Research Department, Bell-Laboratories at Crawford Hill, Holmdel, NJ, USA. Since October 2001, he has been a Full Professor of digital signal processing in mobile communications with Technische Universität Wien, Austria, where he founded the Christian-Doppler Laboratory for Design Methodology of Signal Processing Algorithms, in 2002. Prof. Rupp was an Associate Editor of IEEE TRANSACTIONS ON SIGNAL PROCESSING. He is an Associate Editor of EURASIP Journal on Advances in Signal Processing (JASP) and EURASIP Journal on Embedded Systems (JES).

CHRISTOPH F. MECKLENBRÄUKER (Senior Member, IEEE) received the Dipl.-Ing. (Hons.) degree in electrical engineering from Technische Universität Wien, Vienna, Austria, in 1992, and the Dr.-Ing. (Hons.) degree from Ruhr-Universität Bochum, Bochum, Germany, in 1998. From 1997 to 2000, he was with Siemens AG, Austria, and engaged in the standardization of UMTS. From 2000 to 2006, he was a Senior Researcher with the Telecommunications Research Center Vienna (FTW), Vienna. In 2006, he joined TU Wien, Vienna, as a Full Professor. From 2009 to 2016, he led the Christian Doppler Laboratory for Wireless Technologies for Sustainable Mobility. He has authored approximately 250 papers in international journals and conferences, for which he was also a reviewer and was granted several patents in the field of mobile cellular networks. His research interests include 5G/6G radio interfaces (vehicular connectivity, localization, and sensor networks) and millimeter waves. He is a Member of the Antennas and Propagation Society, Intelligent Transportation Society, Vehicular Technology Society, Signal Processing Society, VDE and EURASIP.